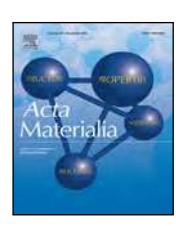


Contents lists available at ScienceDirect

Acta Materialia

journal homepage: www.elsevier.com/locate/actamat



Full length article

Simulations of multivariant Si I to Si II phase transformation in polycrystalline silicon with finite-strain scale-free phase-field approach

Hamed Babaei^a, Raghunandan Pratoori^a, Valery I. Levitas^{a,b,c,*}

- ^a Department of Aerospace Engineering, Iowa State University, Ames, IA 50011, USA
- ^b Departments of Mechanical Engineering, Iowa State University, Ames, IA 50011, USA
- ^c Ames Laboratory, Division of Materials Science and Engineering, Ames, IA 50011, USA

ARTICLE INFO

Keywords: Multivariant martensitic phase transformation Silicon polycrystal Scale-free phase-field approach Finite element simulations Stress-dependent effective threshold Finite strain

ABSTRACT

Scale-free phase-field approach and corresponding finite element method simulations for multivariant martensitic phase transformation from cubic Si I to tetragonal Si II in a polycrystalline aggregate are presented. Important features of the model are large and very anisotropic transformation strain tensor ε_i {0.1753; 0.1753; -0.447} and stress-tensor dependent athermal dissipative threshold for transformation, which produce essential challenges for computations. 3D polycrystals with stochastically oriented grains are subjected to uniaxial strain- and stress-controlled loadings under periodic boundary conditions and zero averaged lateral strains. Coupled evolution of discrete martensitic microstructure, volume fractions of martensitic variants and Si II, stress and transformation strain tensors, and texture are presented and analyzed. Macroscopic variables effectively representing multivariant transformational behavior are introduced. Macroscopic stress-strain and transformational behavior for 55 and 910 grains are close. Large transformation strains and grain boundaries lead to huge internal stresses of tens GPa, which affect microstructure evolution and macroscopic behavior. In contrast to a single crystal, the local mechanical instabilities due to phase transformation and negative local tangent modulus are stabilized at the macroscale by arresting/slowing the growth of Si II regions by the grain boundaries. This leads to increasing stress during transformation. The developed methodology can be used for studying similar phase transformations with large transformation strains and for further development by including plastic strain and strain-induced transformations.

1. Introduction

Silicon is the second most abundant material in the earth's crust. The semiconducting Si I phase (cubic diamond lattice, Fd3m space group) is extensively used in microelectronics, integrated circuits, photovoltaics, and MEMS/NEMS technologies. Single-crystal Si is also used in high-power lasers. Polycrystalline Si is widely used in solar panels [1], thin transistors [2], and very large-scale integration (VLSI) manufacturing. It also has low toxicity and high stability. Due to high demands, the recent CHIPS and Science Act will provide new funding to boost the research and manufacturing of semiconductors in the US. Under the pressure of 10-16 GPa, semiconducting Si I transforms to metallic phase Si II (β -tin structure, $I4_1/amd$ space group). Si I is very strong and brittle, and hence its bulk hardness is 12 GPa and is determined by Si I→Si II phase transformation (PT) rather then dislocational plasticity [3,4]. Stresses exceed 10 GPa for machining (turning, polishing, scratching, etc.) of single and polycrystalline Si [5]; such loads cause plastic flow, Si I→Si II and some other PTs, e.g., amorphization.

High-pressure torsion of Si at 24 GPa is used to produce nanostructured metastable phases [6,7]. Machining of strong brittle semiconducting Si-I is accompanied by microcrack propagation inside the bulk. PT from Si I to ductile and weaker Si II is utilized to develop ductile machining regimes [8], which reduces forces, energy, and damage. This also may eliminate the necessity of using chemical additives during machining, which brings definite environmental benefits by reducing pollution.

Since transformation strain tensor that describes the transformation of cubic to tetragonal Si I \rightarrow Si II PT has large and very anisotropic principal components $\varepsilon_t = \{0.1753; 0.1753; -0.447\}$ [9–11], it is clear from thermodynamics that deviatoric part of the stress tensor should strongly affect this PT. Both pressure- and stress-induced PTs start at pre-existing defects (different dislocation configurations, grain boundaries), which represent stress concentrators. However, in many of the applications, like turning, polishing, scratching, friction, high-pressure torsion and ball milling, PTs occur during plastic deformation. According to classification [12–14], such PTs are called plastic strain-induced PT

^{*} Corresponding author at: Department of Aerospace Engineering, Iowa State University, Ames, IA 50011, USA. E-mail address: vlevitas@iastate.edu (V.I. Levitas).

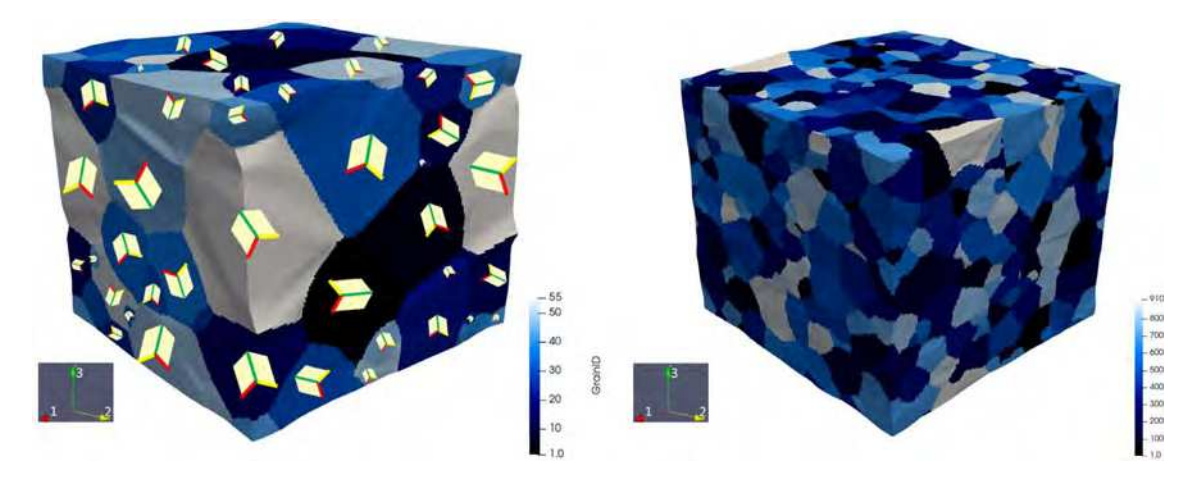


Fig. 1. Grain distribution generated from DREAM.3D for (a) 55 grains showing the local orientations of individual grains (red = 1, yellow = 2, green = 3) and (b) 910 grains. Each grain has a different orientation that is randomly assigned to make sure the sample, on the whole, is texture-free. Files with complete information about orientation of each grain for both samples are given in supplementary material. (For interpretation of the references to color in this figure legend, the reader is referred to the web version of this article.)

under high pressure, and they occur at defects permanently generated during plastic flow. Strain-induced PTs require completely different thermodynamic, kinetic, and experimental treatments than pressure-and stress-induced PTs.

There are numerous very strong effects of plastic deformations on PTs, summarized in [12–18]; one of the most important is a drastic reduction in PT pressure. Thus, plastic strain-induced PTs from graphite to hexagonal and cubic diamonds were obtained at 0.4 and 0.7 GPa, 50 and 100 times lower than under hydrostatic loading, respectively, and well below the phase equilibrium pressure of 2.45 GPa [18]. About an order of magnitude reduction in PT pressure was reported for PT from rhombohedral to cubic BN [19], hexagonal to wurtzitic BN [20], and from α to ω Zr [21,22].

The effect of plastic straining on PTs in Si is also very strong but more sophisticated. Thus, under compression and shear in rotational diamond anvil cell [23], Si II was obtained at 5.2 GPa, but not directly from Si I, but via Si III. However, in these experiments, only optical, pressure, and electric resistivity measurements were utilized without in situ X-ray diffraction. In our recent in situ X-ray diffraction experiments [24], the PTs pressure for direct Si I→Si II PT was reduced from 13.5 (hydrostatic loading) to 2.5 GPa (plastic straining) for micron size Si particles and from 16.2 GPa to 0.4 GPa for 100 nm Si nanoparticles, i.e., by a factor of 40.5 (and 26.3 below the phase equilibrium pressure of 10.5 GPa [25]).

To understand the effect of stress tensor and plastic strain on Si $I\rightarrow Si$ II PT, various techniques at multiple scales are used. With first principle simulations, the lattice instability for Si I under two-parametric loadings was studied in [26–29]. Although it is not specified, it is related to Si $I\rightarrow Si$ II PT. The stress–strain behavior and elastic instabilities leading to Si $I\rightarrow Si$ II PT under all six components of the stress tensor were determined in [30,31]. While this seems to be impossible due to a large number of combinations, the following solution was found. First, the analytical expression for crystal lattice instability criterion was formulated within the phase-field approach (PFA) [10,11,32]. Then it was confirmed and quantified with first principle simulations in [30].

A similar approach was realized earlier with molecular dynamics simulations [10,11] under the action of three normal stresses. Molecular dynamics simulations of PTs in Si during various loadings, nanoindentation, scratching, and surface processing were performed in [4,33–37].

Nanoscale PFA for PT Si $I \rightarrow Si$ II in a single crystal with corresponding simulations was developed in [38–42]. It was calibrated by results of molecular dynamics simulations in [10,11]. The effect of a single dislocation on this PT under uniaxial compression is modeled in [40].

The main general problem with nanoscale PFA is that the width of the martensitic interface is ~ 1 nm and one needs at least 3–5 finite elements within the interface [43], making problem computationally expensive for large samples. Hence this model can be used to treat nano-sized samples only.

Here, we will consider scale-free PFA for modeling discrete martensitic microstructure. It was developed for small strains in [44,45] and updated and applied to NiTi shape memory alloy in [46]. The only finite-strain generalization of the scale-free model for finite strains is presented in [47]. This model was applied for simulations of Si I \rightarrow Si II PT in a single crystal using the finite element method (FEM). The next natural step is to simulate PTs in Si and discrete martensitic microstructure in a polycrystalline sample, which was not done yet and is quite a challenging problem. Actually, we are not aware of PFA simulations of PTs for a polycrystal at large strains for any material.

In this work, we extend the modeling presented in [47] to Si I→Si II PT in 3D polycrystalline samples with up to 1000 grains. The main computational (and constitutive) challenge is to reach convergence of the computational procedure due to strong nonlinearities, large transformation strain localization with large gradients within a singleelement diffuse interface, and elastic instabilities in some grains. For a single crystal, just two loadings, uniaxial and hydrostatic, have been considered in [47]. However, each grain is subjected to different complex and heterogeneous loading in a polycrystal. While we used the simplest quadratic in elastic Lagrangian strain expression (Eq. (7)) for the elastic energy, it is shown in [48] that even simple uniaxial compression leads to elastic instability. This instability can cause additional strain localization and divergence of solution. Due to the variety of heterogeneous complex loadings, different for different grains, chances for various elastic instabilities and divergence are very high. Periodic boundary conditions along the lateral surfaces played important part in the avoiding divergence. Another problem is to adequately quantitatively present the evolution of the local and average volume fraction of martensitic variants; a straightforward approach leads to contradictory

The paper is organized as follows. In Section 2 complete system of coupled PFA and nonlinear mechanics equations is presented. Materials parameters for the model are given in Section 3. Problem formulations, results of simulations, and their analyses are presented in Section 4. Coupled evolution of discrete martensitic microstructure, volume fractions of martensitic variants and Si II, stress and transformation strain tensors, and texture are presented and analyzed. Concluding remarks are summarized in Section 5.

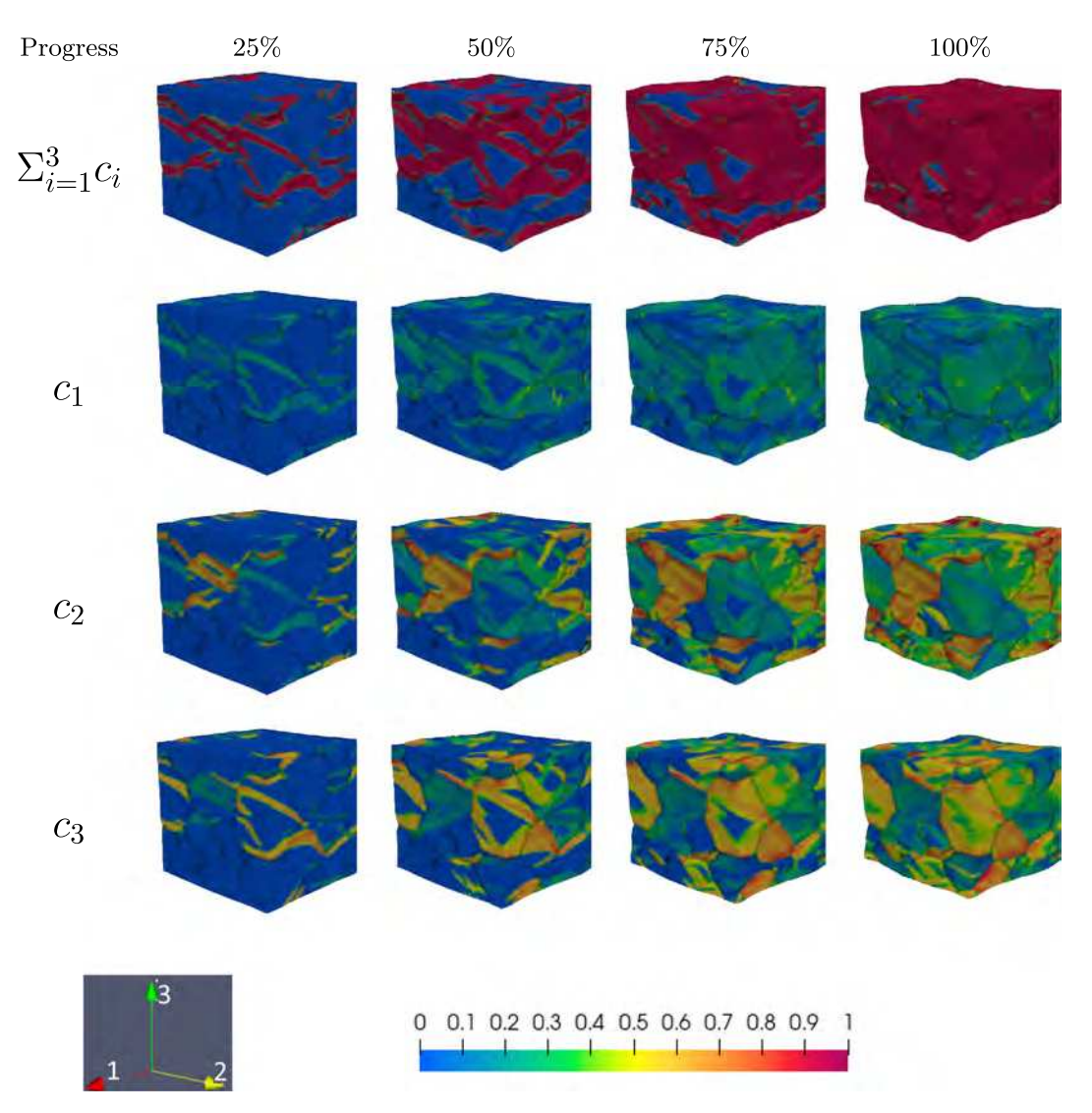


Fig. 2. Evolution of volume fractions of phases for strain-controlled loading of a sample with 55 grains. The figure shows snapshots at different stages of completion of simulation (25%, 50%, 75%, and 100%) in different columns for Si II, c, and each martensitic variant, c_i . (For interpretation of the references to color in this figure legend, the reader is referred to the web version of this article.)

2. Model description

Here, we expand the microscale model for multivariant martensitic PTs developed in [47] for a polycrystalline elastic materials. The main features of the scale-free PFA, which significantly differ it from the traditional nanoscale PFAs are:

1. The energy term that includes gradients of the order parameters and determines the phase interface widths and the interface energies is excluded. This makes the model scale-free. Interface width is getting equal to a single finite element, which is much more computationally economical than in the nanoscale approach, where 3–5 elements are usually required to reproduce analytical solution for an interface [43]. However, this leads to two problems. (a) The solution is mesh dependent. However, detailed computational experiments in [44,45,47] show that the solution becomes practically mesh-independent after the mesh size is 80 times smaller than the sample size. (b) Since the volume fraction of martensite varies from 0 to 1 within the one-element thick interface, for large transformation strains, there are large strain gradients within the interface, which leads often to divergence in the FEM solution.

- 2. The interfaces between individual martensitic variants are not resolved. Each of these variant has a width of $d \simeq 10\,$ nm, i.e., thousands of interfaces at the microscale, making the problem computationally impractical. Here, martensite is considered a mixture of martensitic variants with corresponding volume fractions
- 3. Since there is no need to reproduce atomic level energy land-scape versus order parameters, the linear mixture rule is applied for all material properties. This is in contrast to higher-order polynomials in order parameters for nanoscale PFA. Also, the athermal dissipative threshold for interface propagation (interface friction) can be easily introduced in the scale-free model, while this is a problem for the nanoscale model.
- 4. The volume fraction of the martensite is the order parameter, i.e., it is responsible for the material instability and transformation strain localization at the interface between austenite and martensite. The volume fractions of the individual martensitic variants are only internal variables and do not produce any instabilities. That is how we eliminate interfaces between martensitic variants.

All the above features allow us to economically model multivariant martensitic PTs in a sample of arbitrary size.

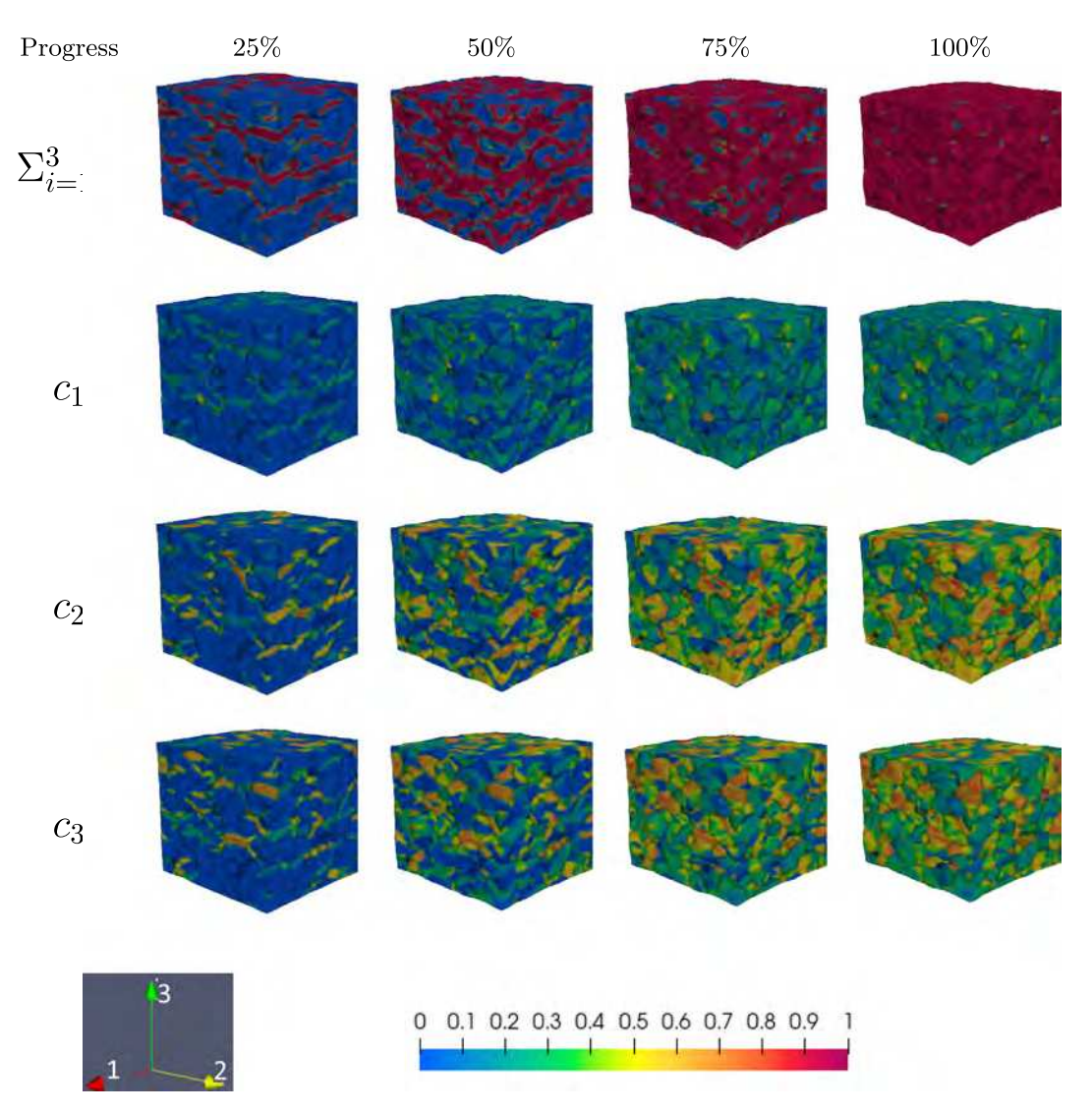


Fig. 3. Evolution of volume fractions for strain-controlled loading of a sample with 910 grains. (For interpretation of the references to color in this figure legend, the reader is referred to the web version of this article.)

Since martensitic variants are in twin relationship with each other, this model automatically includes twinning in the martensite as one of the stress relaxation mechanisms. Note that molecular dynamics simulations in [37] that show twinning in the martensite without dislocation activity reproduce well the Si I-Si II and variant–variant interface orientations.

Vectors and tensors are designated with boldface symbols. We designate contractions of tensors $\mathbf{A} = \{A_{ij}\}$ and $\mathbf{B} = \{B_{ji}\}$ over one and two indices as $\mathbf{A} \cdot \mathbf{B} = \{A_{ij} \ B_{jk}\}$ and $\mathbf{A} : \mathbf{B} = A_{ij} \ B_{ji}$. The transpose of \mathbf{A} is \mathbf{A}^T ; \mathbf{I} is the unit tensor; ∇_0 is the gradient operator in the undeformed state.

2.1. Kinematics

Let us consider polycrystalline Si I aggregate in the undeformed stress-free configuration Ω_0 . The orientation of each grain is characterized by the rotation tensor R_g in the undeformed configuration, which rotates local cubic crystallographic axes of the grain to the global coordinate system. Tensors R_g do not evolve during loading and PTs. The deformation gradient F is multiplicatively split into the elastic F_e and the transformational F_t parts:

$$F = \nabla_0 \mathbf{r} = F_e \cdot F_t; \qquad F_e = R_e \cdot U_e; \qquad F_t = F_t^T. \tag{1}$$

Here, r is the position vector in the current deformed configuration Ω ; F_t is defined as F after complete local stress release (producing the intermediate configuration Ω_t) and is considered to be rotation-free; U_e is the symmetric elastic right stretch tensor and R_e is the orthogonal lattice rotation tensor during loading and PT, which determines texture evolution. The transformation deformation gradient is defined using the mixture rule for m variants as

$$\boldsymbol{F}_{t} = \boldsymbol{I} + \boldsymbol{\varepsilon}_{t} = \boldsymbol{I} + \sum_{i=1}^{m} \boldsymbol{R}_{g} \cdot \tilde{\boldsymbol{\varepsilon}}_{ti} \cdot \boldsymbol{R}_{g}^{T} \boldsymbol{c}_{i}, \tag{2}$$

where ϵ_i is the transformation strain, $\tilde{\epsilon}_{ii}$ is the transformation strain of the *i*th martensitic variant in the local crystallographic basis of the grain, and the c_i is the volume fraction of the *i*th variant in terms of volumes in the reference configuration.

The total, elastic, and transformational Lagrangian strains are defined as

$$\boldsymbol{E} = \frac{1}{2} (\boldsymbol{F}^T \cdot \boldsymbol{F} - \boldsymbol{I}); \quad \boldsymbol{E}_e = \frac{1}{2} (\boldsymbol{F}_e^T \cdot \boldsymbol{F}_e - \boldsymbol{I}); \quad \boldsymbol{E}_t = \frac{1}{2} (\boldsymbol{F}_t^T \cdot \boldsymbol{F}_t - \boldsymbol{I}). \tag{3}$$

Utilization of multiplicative decomposition Eq. (1) results in the following relationship:

$$E_e = F_t^{-1} \cdot (E - E_t) \cdot F_t^{-1}. \tag{4}$$

We will also need the ratios of elemental volumes dV and mass densities ρ in the different configurations, which are described by the

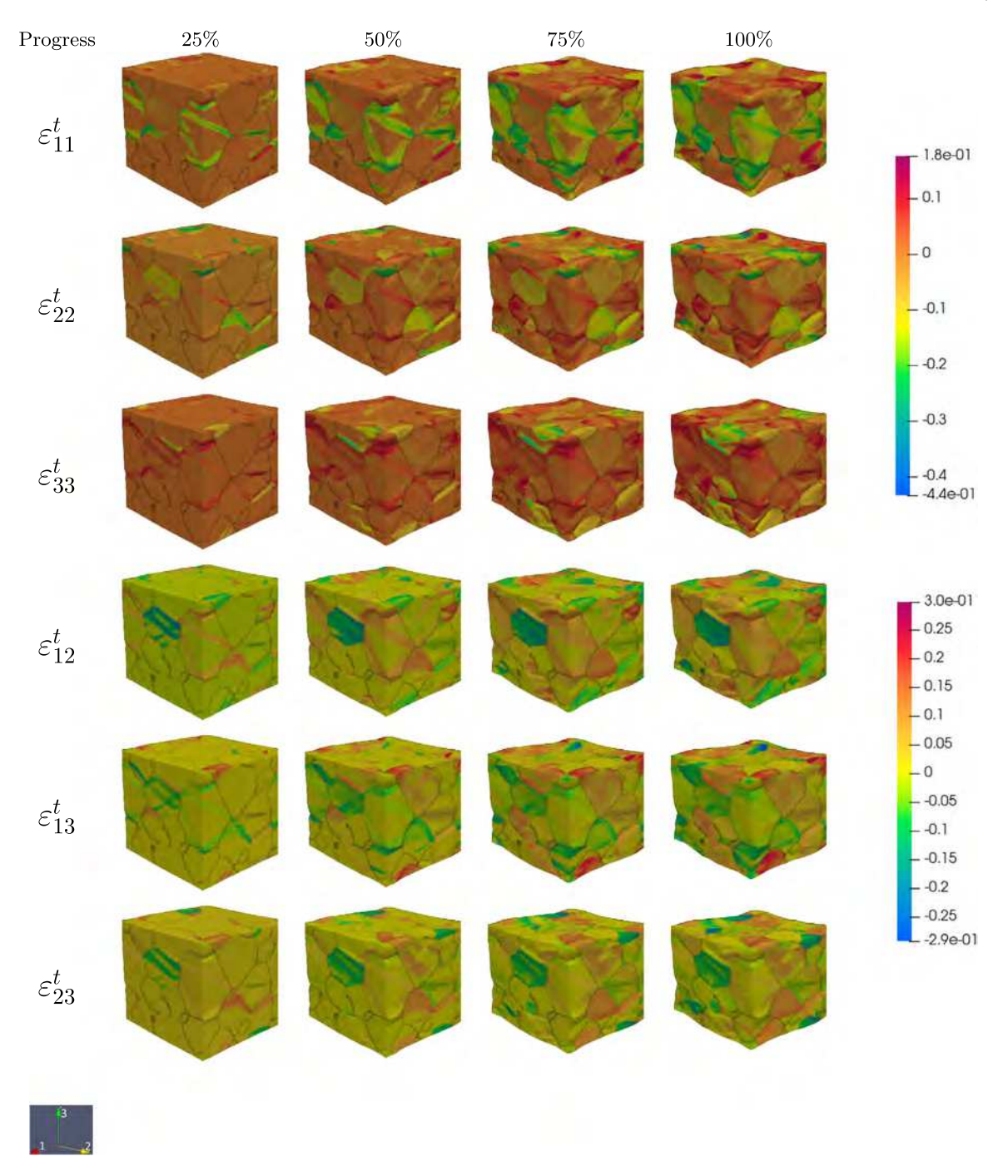


Fig. 4. Evolution of components of the transformation strain tensor ε_t for strain-controlled loading of a sample with 55 grains.

Jacobian determinants:

$$J = \frac{dV}{dV_0} = \frac{\rho_0}{\rho} = \det F;$$

$$J_t = \frac{dV_t}{dV_0} = \frac{\rho_0}{\rho_t} = \det F_t; \quad J_e = \frac{dV}{dV_t} = \frac{\rho_t}{\rho} = \det F_e.$$
 (5)

2.2. Helmholtz free energy

In defining the Helmholtz free energy ψ per unit undeformed volume in Ω_0 of the mixture of austenite and m martensitic variants, contributions from the elastic ψ^e , thermal (or chemical) ψ^θ , and

interaction ψ^{in} energy are given by

$$\psi(F_e, c_i, \theta) = J_i \psi^e(F_e, c_i) + \psi^\theta(\theta, c_i) + \psi^{in}(c_i).$$
 (6)

The elastic energy ψ^e is defined in Ω_t (current configuration), and the Jacobian determinant J_t maps it into Ω_0 (initial configuration). The term $\psi^{in} = \mathcal{A}cc_0 \geq 0$ with c_0 and c for the volume fractions of the austenite and martensite, respectively, includes the interactions between austenite and martensite, the energy of internal stresses, as well as the austenite–martensite phase interface energy; interaction between martensitic variants is neglected to avoid formation of variant–variant interfaces. Positive $\mathcal A$ results in a negative tangent modulus of the equilibrium stress–strain curve during PT [44,45,47], which results in local mechanical instability and the formation of the localized

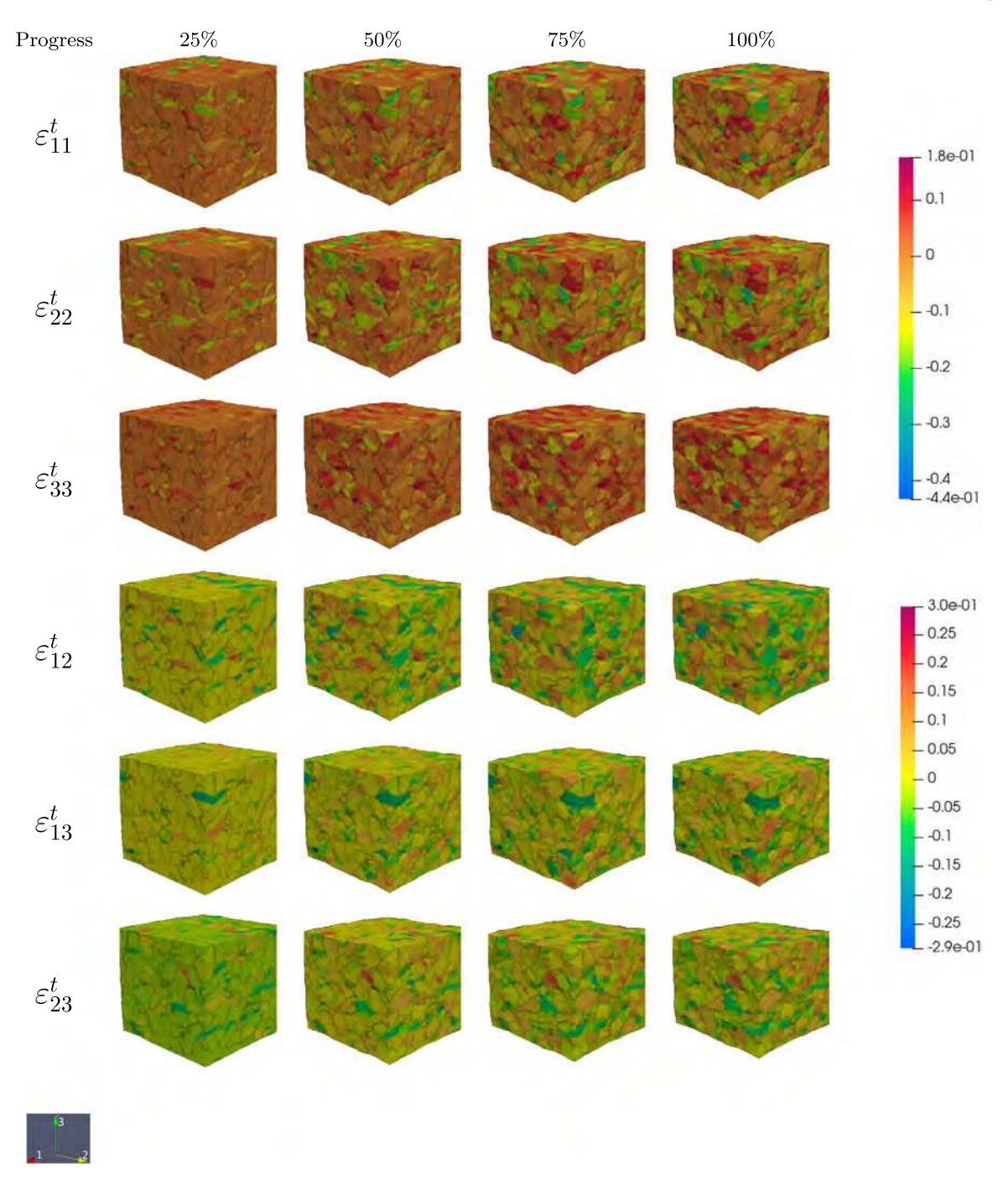


Fig. 5. Evolution of the components of the transformation strain tensor ϵ_i for strain-controlled loading of a sample with 910 grains.

transformation bands/regions of the product phase. In such a way, a discrete martensitic structure is reproduced, similar to the nanoscale PFA. The thermal (chemical) free energy ψ^θ is the free energy at zero applied stresses and neglected interaction between phases. It depends on the temperature θ and volume fractions of all phases.

The elastic energy is expressed as

$$\psi^{e} = \frac{1}{2} E_{e} : \tilde{C} : E_{e} = \frac{1}{2} \tilde{C}^{ijkl} E_{e}^{ij} E_{e}^{kl}; \qquad \tilde{C}^{ijkl} = \sum_{p=0}^{m} \tilde{C}_{p}^{ijkl} c_{p}, \tag{7}$$

where the components of the fourth-rank elastic moduli tensor \tilde{C}_p^{ijkl} in the global coordinate system are defined in terms of components in the local for each grain crystallographic system C_p^{rqnm} and grain rotations

$$R_g^{ml}$$
 :

$$\tilde{C}_p^{ijkl} = R_g^{lm} R_g^{kn} R_g^{jq} R_g^{ir} C_p^{rqnm}.$$
(8)

Since the thermal energy of all martensitic variants is the same, $\psi_i^{\,\theta}=\psi_i^{\,\theta}=\psi_M^{\,\theta}$, the thermal energy of the mixture is

$$\psi^{\theta} = \sum_{i=0}^{m} c_i \psi_i^{\theta}(\theta) = c_0 \psi_A^{\theta}(\theta) + c \psi_M^{\theta}(\theta); \qquad c = \sum_{i=1}^{m} c_i; \qquad c_0 = 1 - c, \quad (9)$$

where $\psi_0^\theta = \psi_A^\theta$ is the thermal energy of austenite.

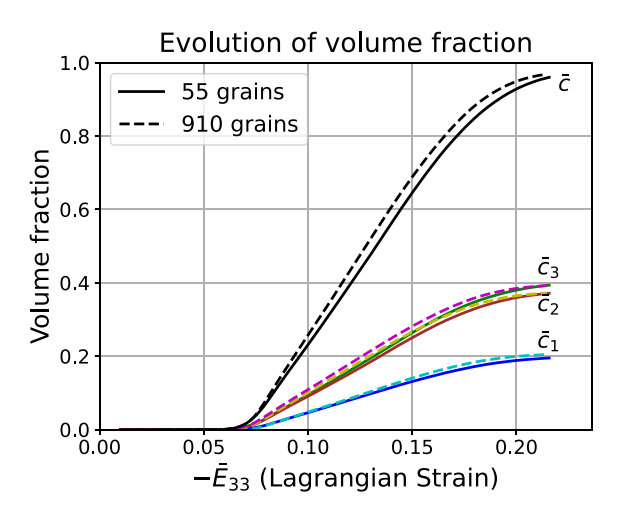


Fig. 6. Volume fraction of each martensitic variant (\bar{c}_i) and the total martensite (\bar{c}) averaged over the sample based on Eq. (17) vs. strain for strain-controlled loading. The lack of physical sense for \bar{c}_i is described in the text.

2.3. Dissipation inequality

The Plank's inequality for isothermal processes is

$$D = \mathbf{P}^T : \dot{F} - \dot{\psi} \ge 0, \tag{10}$$

where D is the dissipation rate per unit undeformed volume; P is the first Piola–Kirchhoff stress. After traditional thermodynamic manipulations, D can be expressed as the product of the thermodynamic driving forces for $A \rightarrow M_i, X_{i0}$, and $M_j \rightarrow M_i, X_{i0}$, transformations and conjugate rates:

$$D = \sum_{i=1}^{m} X_{i0} \dot{c}_{i0} + \sum_{j=1}^{m-1} \sum_{i=j+1}^{m} X_{ij} \dot{c}_{ij} \ge 0;$$

$$X_{i0} = W_{i0} - \frac{J_{t}}{2} E_{e} : (\bar{C}_{i} - \bar{C}_{0}) : E_{e} - \frac{J_{t}}{2} (E_{e} : \bar{C}(c) : E_{e}) F_{t}^{-1}$$

$$: \varepsilon_{ti} - \Delta \psi^{\theta} - A(1 - 2c);$$

$$X_{ij} = W_{ij} - \frac{J_{t}}{2} E_{e} : (\bar{C}_{i} - \bar{C}_{j}) : E_{e} - \frac{J_{t}}{2} (E_{e} : \bar{C}(c) : E_{e}) F_{t}^{-1} : (\varepsilon_{ti} - \varepsilon_{tj});$$

$$W_{i0} = P^{T} \cdot F_{e} : \varepsilon_{ti} = J F_{e}^{T} \cdot \sigma \cdot F_{e}^{t-1} \cdot F_{t}^{-1} : \varepsilon_{ti};$$

$$W_{ij} = P^{T} \cdot F_{e} : (\varepsilon_{ti} - \varepsilon_{tj}) = J F_{e}^{T} \cdot \sigma \cdot F_{e}^{t-1} \cdot F_{t}^{-1} : (\varepsilon_{ti} - \varepsilon_{tj}). \tag{11}$$

Here, \dot{c}_{i0} and \dot{c}_{ij} are the rate of change of volume fraction of variant i due to transformation to the austenite and variant j, respectively; W_{i0} is the transformation work for austenite to martensite PT, W_{ij} is the transformation work for variant j to variant i transformation, $\Delta \psi^{\theta}$ is the jump in thermal free energy during transformation, and $\sigma = J^{-1} P \cdot F^T$ is the Cauchy (true) stress tensor.

While the PFA does not explicitly includes phase interfaces, they appear as a result of the solution of the boundary-value problem. Then one can derive the expression for the thermodynamic driving force for the austenite–martensite interface propagation, see [47]:

$$X_{\Sigma} = \sum_{i=1}^{m} \frac{c_{i}}{c} \tilde{X}_{i0} = \sum_{i=1}^{m} \tilde{c}_{i} \tilde{X}_{i0} = P^{T} \cdot F_{e} : \epsilon_{tM} - \frac{J_{t}}{2} E_{e}$$

$$: (C_{M} - C_{0}) : E_{e} - \frac{J_{t}}{2} \left(E_{e} : C(c) : E_{e} \right) F_{t}^{-1} : \epsilon_{tM} - \Delta \psi^{\theta};$$

$$\epsilon_{tM} = \sum_{i=1}^{m} \tilde{c}_{i} \epsilon_{ti}; \qquad C_{M} = \sum_{i=1}^{m} \tilde{c}_{i} C_{i}, \tag{12}$$

where $\tilde{c_i} = c_i/c$ is the volume fraction of M_i within martensitic mixture, thus $\sum_{i=1}^m \frac{c_i}{c} = 1$. This expression is obtained from the expression for the dissipation rate due to the austenite–martensite PTs at the phase interface $D_{A-M} = X_{\Sigma}\dot{c}$. It is shown in [47] that for the stationary phase interface X_{Σ} is equal to the athermal threshold for the austenite–martensite interface propagation.

2.4. Kinetic equations

The kinetic equations are formulated as follows for the $A \leftrightarrow M_i$ PTs

$$\begin{cases} \dot{c}_{i0} = \lambda_{i0}(X_{i0} - k_{i-0}) & \text{if } \{X_{i0} - k_{i-0}(c_i, \sigma_i) > 0 \ \& \ c_i < 1 \ \& \ c_0 > 0\} \\ \dot{c}_{i0} = \lambda_{i0}(X_{i0} + k_{i-0}) & \text{if } \{X_{i0} + k_{i-0}(c_i, \sigma_i) < 0 \ \& \ c_i > 0 \ \& \ c_0 < 1\} \\ \dot{c}_{i0} = 0 & \text{otherwise}; \qquad i = 1, 2, \dots, m, \end{cases} \qquad M_i \rightarrow A$$

(13)

and for $M_i \leftrightarrow M_i$ PTs

$$\begin{cases} \dot{c}_{ij} = \lambda_{ij} X_{ij} & \text{if } \{X_{ij} > 0 \& c_i < 1 \& c_j > 0\} \\ & \text{or } \{X_{ij} < 0 \& c_i > 0 \& c_j < 1\} \\ \dot{c}_{ij} = 0 & \text{otherwise;} \end{cases} \quad i \to j \\ \text{otherwise;} \quad i, j = 1, 2, \dots, m,$$
 (14)

where k_{i-0} is the athermal threshold and λ_{i0} and λ_{ij} are the kinetic coefficients. We neglect the athermal threshold for $Mj \leftrightarrow M_i$ PTs. The non-strict inequalities for the volume fraction of phases in Eqs. (13)–(14) imply that the PT from any phase does not occur if the parent phase does not exist or if the product phase is complete.

2.5. Macroscopic parameters

Macroscopic Cauchy stress and the first Piola–Kirchhoff stress, the deformation gradient, transformation strain, and volume fraction of Si II and each martensitic variant, averaged over the sample, are defined as [49–51]

$$\bar{\sigma} = \frac{1}{V} \int_{V} \sigma dV; \qquad \bar{P} = \frac{1}{V_0} \int_{V_0} P dV_0; \tag{15}$$

$$\bar{F} = \frac{1}{V_0} \int_{V_0} F dV_0; \qquad \bar{F}_t \simeq \frac{1}{V_0} \int_{V_0} F_t dV_0; \qquad \bar{\varepsilon}_t \simeq \frac{1}{V_0} \int_{V_0} \varepsilon_t dV_0; \quad (16)$$

$$\bar{c} = \frac{1}{V_0} \int_{V_0} c dV_0; \qquad \bar{c}_i = \frac{1}{V_0} \int_{V_0} c_i dV_0.$$
 (17)

For the Cauchy stress and the first Piola–Kirchhoff stress, the deformation gradient, and volume fractions c and c_i , averaging equations are strict; for the transformation deformation gradient and strain, they are approximate because, in the unloaded stress-free state, they generally are not compatible due to residual elastic strain. We use Eq. (16) because the exact equation is quite bulky and is for F_i instead of F_i . Eq. (17) for c_i , while formally correct, is misleading (Section 4.2). Other macroscopic parameters are defined via \bar{F} and \bar{P} by equations similar to the corresponding local equations:

$$\bar{\boldsymbol{\sigma}} = (\det \bar{\boldsymbol{F}})^{-1} \bar{\boldsymbol{P}} \cdot \bar{\boldsymbol{F}}^T; \qquad \bar{\boldsymbol{E}} = \frac{1}{2} (\bar{\boldsymbol{F}}^T \cdot \bar{\boldsymbol{F}} - \boldsymbol{I}). \tag{18}$$

Eq. (18) for the Cauchy stress is used instead of Eq. (15) because integration over the fixed parallelepiped with regular cubic mesh is much simpler and faster than the integration over the deformed volume.

3. Model parameters

The material parameters required for the implementation of the model, the same as in [47], are presented in Section 2 are listed in Table 1. The transformation strain tensors are taken from the MD simulations in [10,11], and in the local crystallographic axes for all three variants are given by

$$\varepsilon_{t1} = \begin{pmatrix}
0.1753 & 0 & 0 \\
0 & 0.1753 & 0 \\
0 & 0 & -0.4470
\end{pmatrix}; \quad \tilde{\varepsilon}_{t2} = \begin{pmatrix}
0.1753 & 0 & 0 \\
0 & -0.4470 & 0 \\
0 & 0 & 0.1753
\end{pmatrix}; \\
\tilde{\varepsilon}_{t3} = \begin{pmatrix}
-0.4470 & 0 & 0 \\
0 & 0.1753 & 0 \\
0 & 0 & 0.1753
\end{pmatrix}. \tag{19}$$

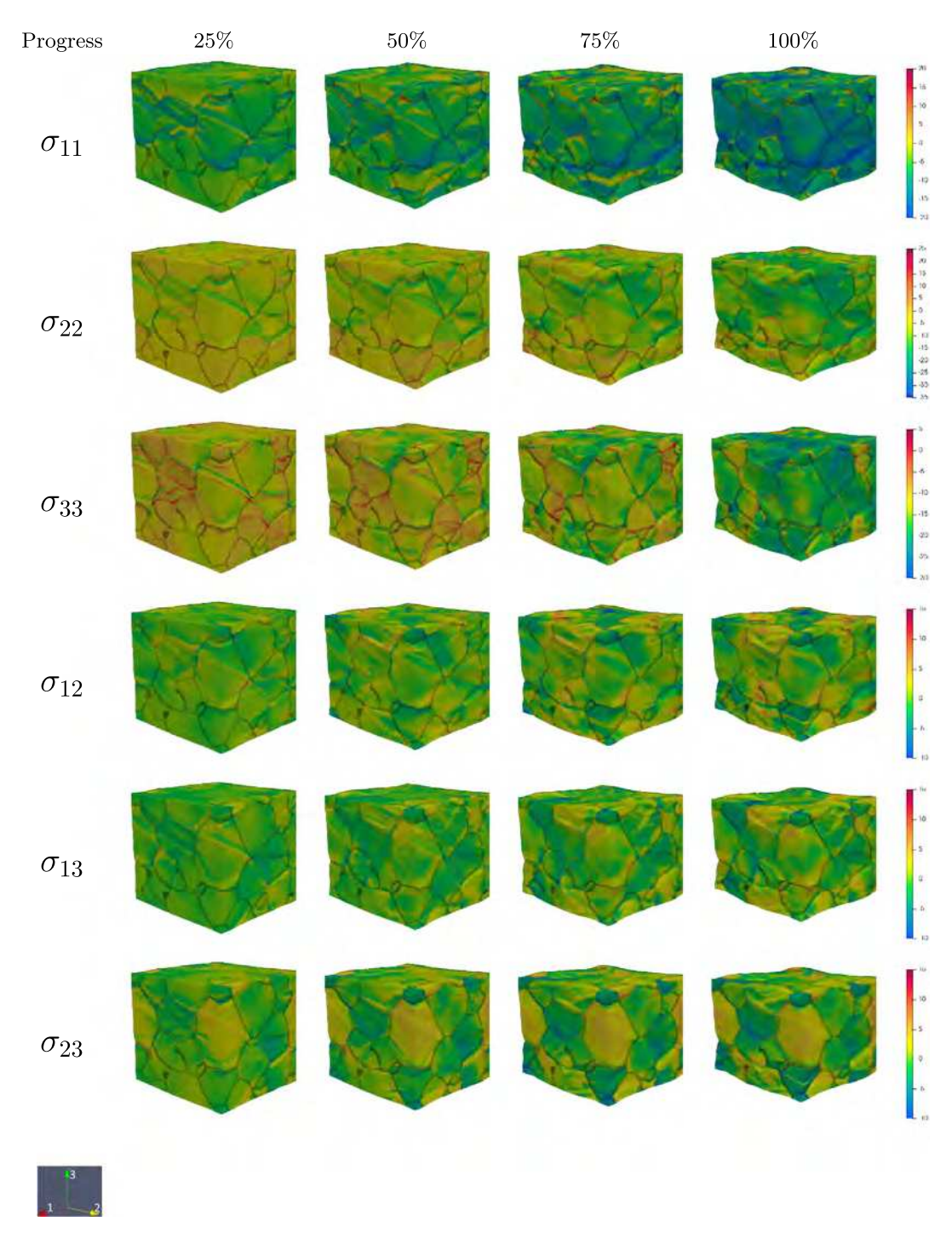


Fig. 7. Evolution of components of the Cauchy stress tensor for strain-controlled loading of a sample with 55 grains.

The elastic constants for both phases are collected from [31,52]. The constants C_0^{ij} in Table 1 denote the independent elastic constants of the austenite, and C_1^{ij} denote those of the first variant of the martensite, both in the local crystallographic axes. The components of the tensor of elastic moduli C^{ijkl} can be calculated using

$$C^{ijkl} = \sum_{n=1}^{3} [\lambda^n \delta^{in} \delta^{jn} \delta^{kn} \delta^{ln} + \mu^n (\delta^{in} \delta^{jn} \delta^{kl} + \delta^{ij} \delta^{kn} \delta^{ln}) + \nu^n (\delta^{in} \delta^{jk} \delta^{ln} + \delta^{jn} \delta^{ik} \delta^{ln} + \delta^{in} \delta^{jl} \delta^{kn} + \delta^{jn} \delta^{il} \delta^{kn})],$$
(20)

where δ^{in} is the Kronecker delta ($\delta^{in}=1$ for i=j and $\delta^{in}=0$ for $i\neq j$), λ^n , μ^n and ν^n for a cubic and tetragonal crystal lattice are given by Eqs. (21) and (22), respectively:

$$\lambda^{1} = \lambda^{2} = \lambda^{3} = C^{11} - C^{12} - 2C^{44},$$

$$2\mu^{1} = 2\mu^{2} = 2\mu^{3} = C^{12},$$

$$2\nu^{1} = 2\nu^{2} = 2\nu^{3} = C^{44}.$$
(21)

$$\lambda^{1} = \lambda^{2} = C^{11} - (C^{12} + 2C^{66}),$$

$$\lambda^{3} = C^{33} + C^{12} + 2C^{66} - 2(C^{13} + 2C^{44}),$$

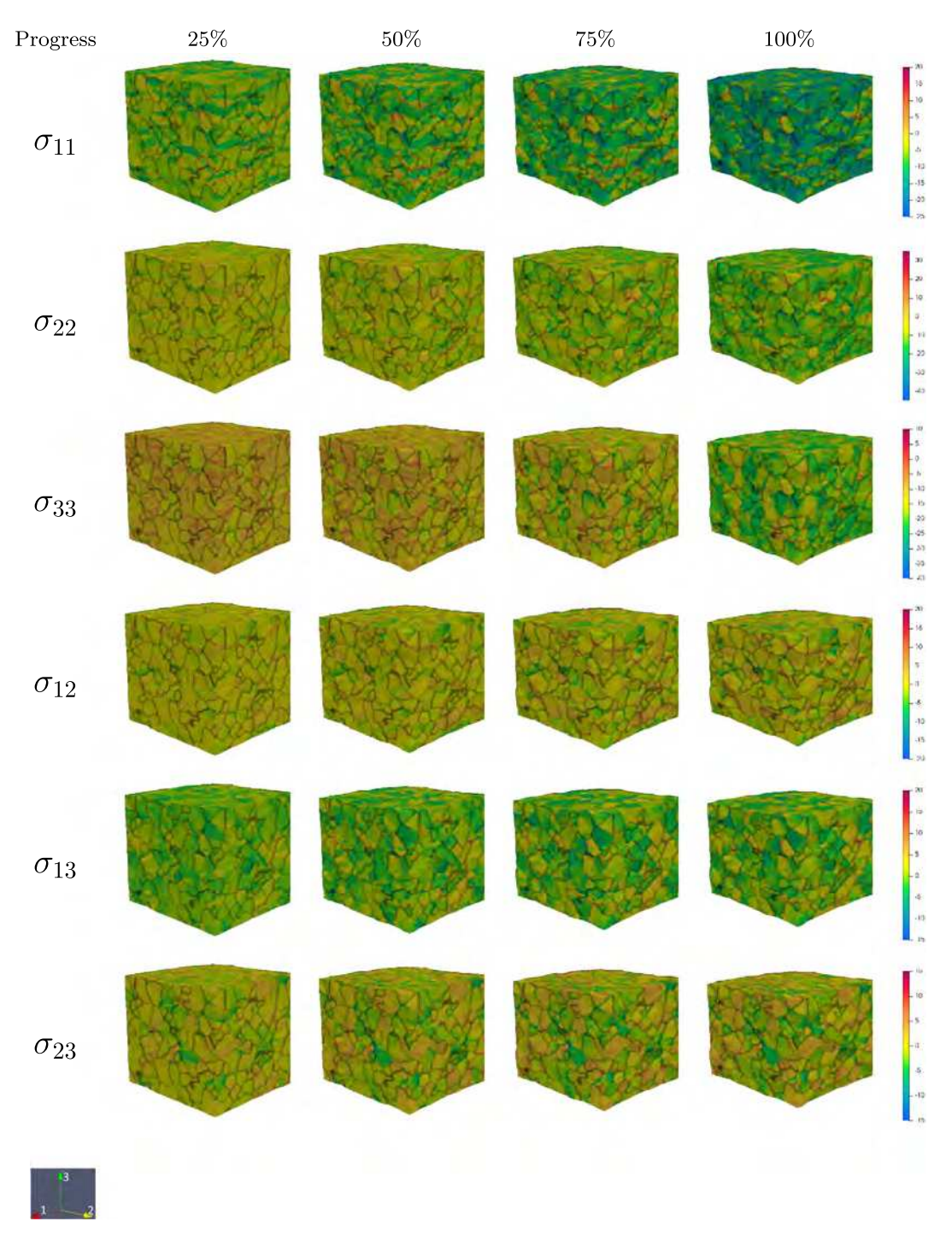


Fig. 8. Evolution of the components of the Cauchy stress tensor for strain-controlled loading of a sample with 910 grains.

$$2\mu^{1} = 2\mu^{2} = C^{12},$$
 $2\mu^{3} = 2C^{13} - C^{12},$
 $2\nu^{1} = 2\nu^{2} = C^{66},$ $2\nu^{3} = 2C^{44} - C^{66}.$ (22)

Under hydrostatic conditions, the phase equilibrium pressure $p_0^{eq}=10.5$ GPa [25] at $J_t=0.764$. The jump in the thermal energy $\Delta\psi^\theta=-p_0^{eq}(J_t-1)=2.47$ GPa, where elastic strain and change in elastic moduli are neglected. Localization of strain is required to reproduce discrete microstructure. As noted in [47], to obtain strain localization, the strain rate should be commensurate with the rate of transformation.

The kinetic coefficient λ and interaction parameter A are selected to ensure that this condition is satisfied.

It is found with the first principle and molecular dynamics simulations [10,11,30] that the criteria for Si I \leftrightarrow Si II PTs are linearly dependent on the Cauchy stress components normal to the cubic faces. We assume the same for the microscale experiments, where the role of defects is effectively included. For cubic to tetragonal PTs, the PT criteria are given by [40,47]

$$A \rightarrow M_i$$
: $a^d(\sigma_1 + \sigma_2) + b^d\sigma_3 > c^d$;

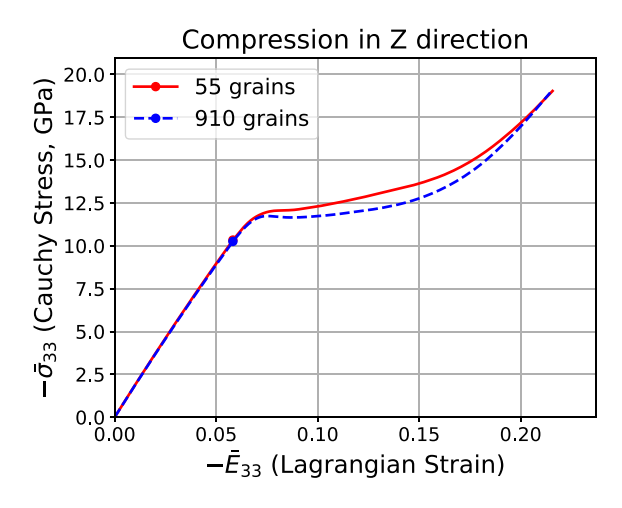


Fig. 9. Averaged Cauchy stress–Lagrangian strain plot for strain-controlled loading for 55 grains and 910 grains. The dot marker represents the onset of phase transformation.

Table 1 Material parameters including kinetic coefficient λ (Pa s)⁻¹, dimensionless constants in the expression for effective thresholds, as well as interaction coefficient A, jump in the thermal energy $\Delta \psi^{\theta}$, and elastic constants, all in GPa.

λ	\boldsymbol{A}	$\Delta\psi^{ heta}$	d_1	d_3	r_1	r_3		
0.02	2	2.47	0.082	0.111	-0.90	0.338		
C_0^{11}	C_0^{44}	C_0^{12}	C_1^{11}	C_1^{33}	C_1^{44}	C_1^{66}	C_1^{12}	C_{1}^{13}
167.5	80.1	65.0	174.76	136.68	60.24	42.22	102.0	68.0

$$M_i \to A$$
: $a^r(\sigma_1 + \sigma_2) + b^r \sigma_3 < c^r$, (23)

where a^d , b^d , c^d , a^r , b^r and c^r are constants determined empirically. To make the thermodynamic PT conditions consistent with experimental conditions, the athermal threshold k_{i-0} is considered to be stress and volume fraction dependent, as described in detail in [47], and calculated based on the relations

$$\begin{aligned} k_{i-0} &= J[a_1(c_i)(\sigma_1 + \sigma_2) + a_3(c_i)\sigma_3]; \\ a_k(c_i) &= d_k + (r_k - d_k)c_i; \quad k = 1 \text{ and } 3, \end{aligned} \tag{24}$$

where d_k and r_k are the fitting parameters, given in Table 1. They are determined by substituting expressions for k_{i-0} from Eq. (24) in the transformation criteria in Eq. (13) with the driving forces from Eq. (11) and some empirical data.

4. Study of multivariant microstructure evolution

A finite element implementation of the scale-free model is developed in the open-source FEM code deal.II [53] using 8-noded 3D cubic linear elements with first-order interpolation and full integration. For such elements, calculations of volume averaged of any parameter a in the undeformed configuration is the sum of values a in each quadrature point divided by the number of quadrature points. Microstructure evolution is studied for polycrystalline samples containing two different numbers of grains, 55 and 910, as shown in Fig. 1. The total number of the finite elements and integration points were \approx 2.1 million and \approx 16.7 million, respectively, for both cases. If we consider position vector r and volume fractions c_1 , c_2 , and c_3 as the primary independent variables, then the total number of degrees of freedom is six times the number of the integration points.

A 3D unit cube sample is constructed in DREAM.3D [54] with the required number of grains. Each grain in the sample is assigned an orientation randomly so that the overall sample remains texture free. Grain boundaries represent 2D surfaces of zero thickness (otherwise, the model will not be scale free), as in most polycrystalline models,

even at nanoscale [55,56]. These are surfaces of jump of all orientation-dependent material properties, like elastic moduli and transformation strain tensors. As we will see in simulations, these jumps produce both stress concentrations for the nucleation of martensite and obstacles for PT transfer from grain to grain.

Two types of compression are applied, strain-controlled and stresscontrolled. For both cases, periodic boundary conditions are applied in directions 1 and 2 with averaged zero averaged strains in these directions. Application of the periodic boundary conditions significantly simplified elimination of divergence of the computational procedure in comparison with other conditions. Such conditions are realized when Si is clamped in the 1-2 plane; a thin Si layer is attached to the rigid substrate, or within a shock wave. For the strain-controlled case, periodic boundary conditions are applied in the direction 3 as well, and a sample is subjected to a uniaxial compressive averaged strain in direction 3. For the stress-controlled loading, on the external planes orthogonal to axis 3, the sample is subjected to homogeneous compressive normal Cauchy stress in the deformed configuration with zero shear stresses, i.e., like under the action of the liquid. Stresscontrolled loading ends with constant "pressure in liquid" of 11 GPa. In total, four simulations are run with two different numbers of grains and two different loading conditions.

4.1. Elastic instabilities, convergence, and periodic boundary conditions

Due to finite elastic strains and various complex loadings for different grains, elastic instabilities may occur even for the simplest expression (Eq. (7)) for the elastic energy, as shown in [48] for the uniaxial compression. Elastic instability at finite strains is determined by the condition [26,57,58]

$$det \left[B^{ijkl} \right] \le 0 \tag{25}$$

with the effective elastic moduli

$$B^{ijkl} = \tilde{C}^{ijkl} - \sigma^{ij}\delta^{kl} + \frac{1}{2}(\sigma^{il}\delta^{jk} + \sigma^{ik}\delta^{jl} + \sigma^{kj}\delta^{li} + \sigma^{lj}\delta^{ki}). \tag{26}$$

Here, \tilde{C}^{ijkl} are the components of the fourth-rank elastic moduli tensor from the expression for the elastic energy Eq. (7). The tensor B^{ijkl} was introduced in [59] as the coefficients in the relationship between stresses and small strains of the pre-deformed crystals and in [60] as the derivative of the Cauchy stress with respect to small strain increment from the current configuration. It is shown in [61] that B^{ijkl} can also be determined from the relationship between the Jaumann derivative of the Cauchy stress σ^{ij} and deformation rate d^{kl} which are used as an input in various computational codes (e.g., ABAQUS or deal.II) for nonlinear elastic problems.

Our preliminary simulations with the constant Cauchy stresses at the lateral surfaces of the sample instead of periodic boundary conditions had a divergence problem. Checking the elastic instability conditions, Eqs. (25) and (26) confirmed that they are satisfied in some finite elements. While after meeting the instability conditions related to the PT (inequalities in Eq. (13)), the system evolves according to kinetic Eq. (13), after losing elastic stability, there is no kinetic equation for the elastic deformation rate that will govern the evolution of the system to the new elastically stable state, which is also unknown. That is why numerical solution diverges. Attempts to resolve the problems by adding viscous stresses after reaching local instabilities were unsuccessful and were not further used. Convergence was achieved only after applying periodic boundary conditions along the lateral sample surfaces. Periodic conditions significantly limit the possibility of system deformation in the lateral directions and suppress elastic instabilities. Locally, periodic conditions result in stresses for which elastic instability conditions Eqs. (25) and (26) are not met. While periodic conditions allow us to perform current studies, there is a clear need to further address this problem for the general stress states, including elastic instabilities. This requires studying these instabilities

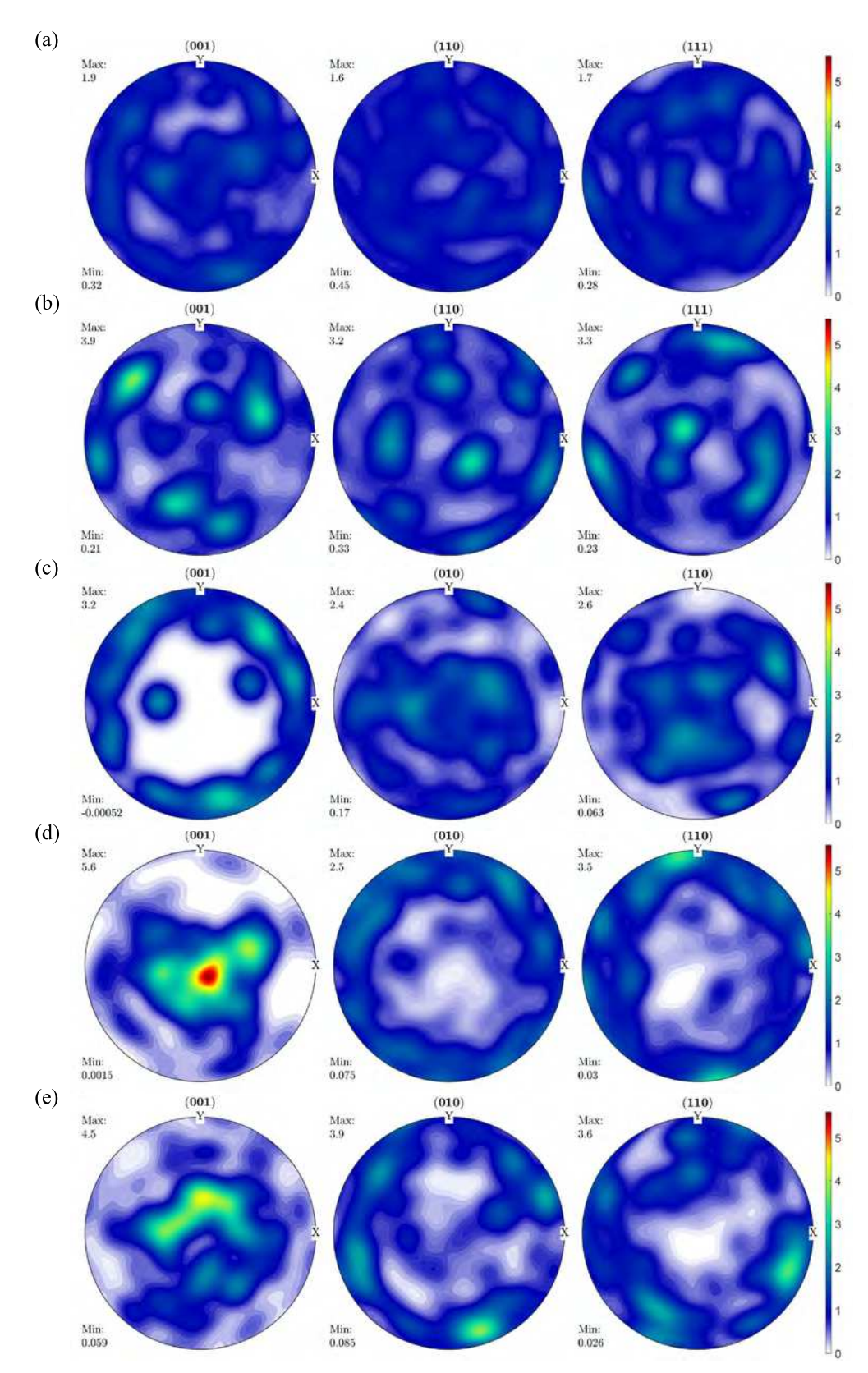


Fig. 10. Pole figures of (a) initial austenite, (b) residual austenite, (c) final martensitic variant M_1 , (d) M_2 , and (e) M_3 for strain-controlled loading of 55 grains. The minimum and maximum intensities for each direction are shown in the legend corresponding to each figure.

and, if they cannot be avoided, developing the constitutive equations that connect them with \dot{c}_{i0} for describing the kinetics of PTs in a way

that the system evolves toward martensitic variants without divergence. This problem will be addressed in the future.

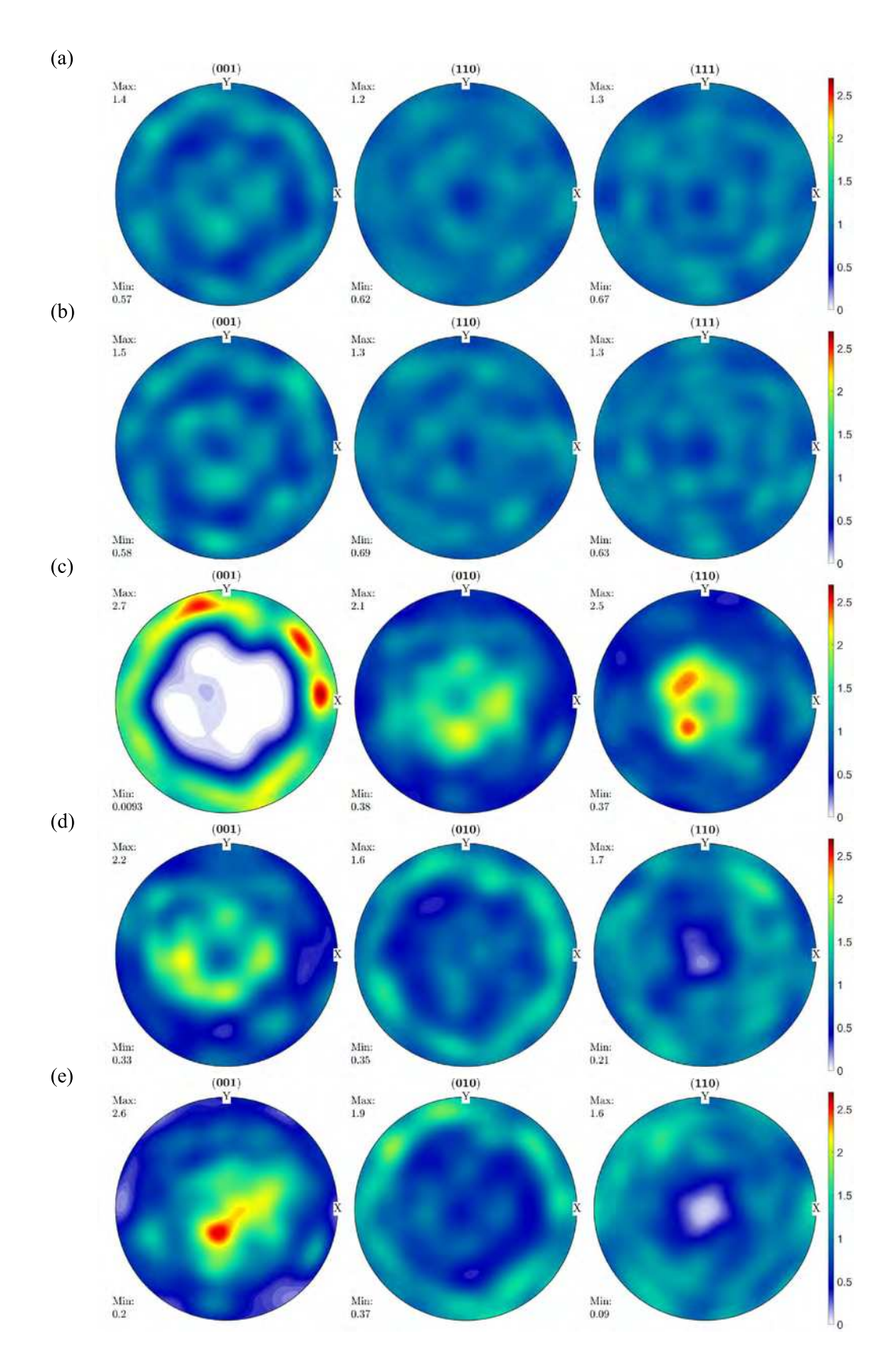


Fig. 11. Pole figures of (a) initial austenite, (b) residual austenite, (c) final martensitic variant M_1 , (d) M_2 , and (e) M_3 for strain-controlled loading of 55 grains. The minimum and maximum intensities for each direction are shown in the legend corresponding to each figure.

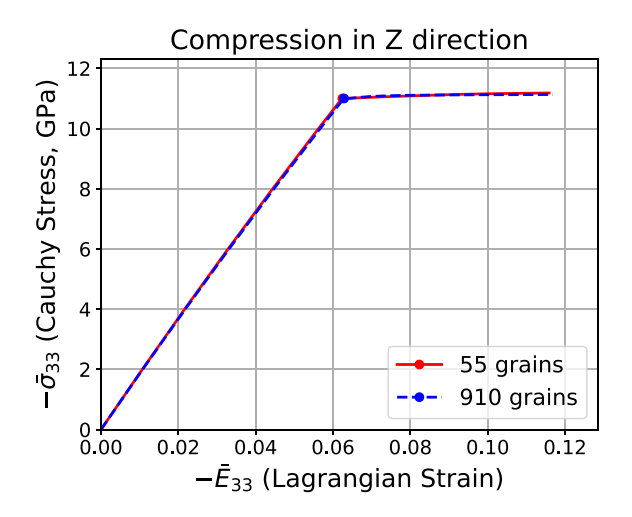


Fig. 12. True stress-strain plot for stress-controlled loading for 55 and 910 grains. The dot marker represents the onset of phase transformation.

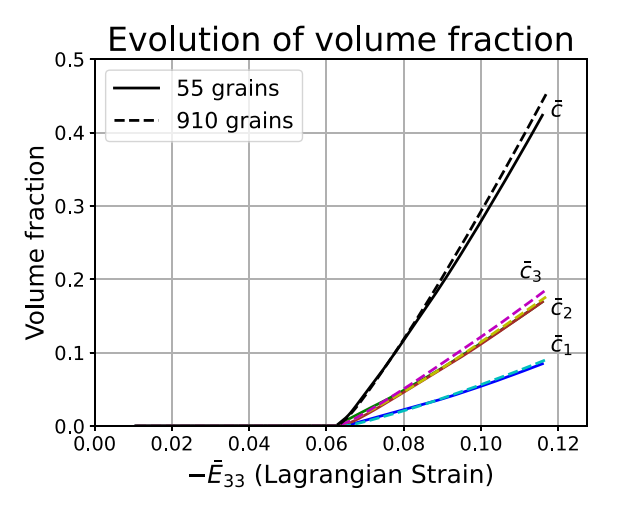


Fig. 13. Volume fraction of each martensitic variant $\bar{c_i}$ and total martensite \bar{c} averaged over the sample based on Eq. (17) vs. strain for stress-controlled loading. The lack of physical sense for $\bar{c_i}$ is described in the text.

4.2. Strain-controlled loading

For strain-controlled loading, the initial strain rate used, in the elastic regime, is $1 \times 10^{-2} \text{ s}^{-1}$ and reduced to $5 \times 10^{-5} \text{ s}^{-1}$ once the material starts to transform. While we can choose any strain rate, such low strain rates are chosen because they are not achievable in atomistic simulations. Figs. 2 and 3 show the evolution of martensite at three intermediate stages (25%, 50%, and 75% of the simulation) and the final stage of the simulation. The first row shows the total volume fraction of martensite c followed by those for individual martensitic variants. The black lines in Figs. 2 and 3 outline the grain boundaries for all the grains. The videos demonstrating the evolution of the volume fractions are provided in the supplementary material. Volume fractions of each martensitic variant \bar{c}_i and martensite \bar{c} averaged over the sample based on Eq. (17) vs. strain are shown in Fig. 6. Nucleation starts mostly at the grain boundaries and triple junctions, which represent stress concentrators. Nucleation starts with the dominant variant, which produces maximum transformation work; two other variants appear in the same regions to accommodate the transformation strain and reduce internal stresses. A similar proportion between variants remains during further growth. In grains with different orientations, growth occurs either along the grain boundaries or inside the grain,

which is arrested either at grain boundaries or other martensitic units. The general trend is that the lower-angle grain boundaries produce lower stress concentration for nucleation of martensitic variants but lower resistance for martensitic units to pass from grain to grain. The larger-angle grain boundaries produce large stress concentration and cause nucleation and growth of the martensite along the grain boundary but strongly resist or prevent passing transformation to the neighboring grain. In each unit full transformation to Si II occurs quickly, thus forming discrete Si II microstructure, as desired. With increasing strain, both Si II broadening of existing Si II regions and the appearance of new nuclei occur. At the end of the loading, PT is completed almost everywhere, with small residual Si I pockets. They are caused by internal stresses due to large transformation strains. For both numbers of grains, \bar{c} saturates at 96%.

It can be clearly seen from Figs. 2, 3 and 6 that the second and the third variants are dominating over the first one, which looks contradictory. To better understand the reasons for these results, let, for simplicity and illustration, consider 5 grains: grain 1 oriented with [100] direction along axis 3 (variant 1); grains 2 and 3, rotated by $\pm 90^{\circ}$ about axis 1 (variant 1), and grains 4 and 5, rotated by $\pm 90^{\circ}$ about axis 2 (variant 3). Due to symmetry, this is still the same single crystal. If we treat it like a single crystal and transform it homogeneously till completion, we obtain $c_1=1$, $c_2=c_3=0$, and $\epsilon_t=\epsilon_{t1}$. However, if we treat it as a polycrystal, in grain 1, we will have the same $c_1 = 1$, $c_2 = c_3 = 0$ and $\epsilon_t = \epsilon_{t1}$. In the local coordinate system of grains 2 and 3, this transformation strain looks like $\varepsilon_t = \varepsilon_{t2}$, i.e., $c_2 = 1$, $c_1 = c_3 = 0$. Similarly, in the local coordinate system of grains 4 and 5, the transformation strain is ε_{t3} , i.e., $c_3 = 1$, $c_1 = c_2 = 0$. After averaging these volume fractions over the entire sample, we obtain $c_1 = 1/5$, $c_2 = c_3 = 2/5$, what we approximately observe in Fig. 6. The main point is that c_i for each grain does not have a lot of sense unless the orientation of the grain is shown. That is why we give complete information about orientation of each grain in supplementary material and show orientations in Fig. 1a. The average over the sample \bar{c}_i does not have any physical sense because the orientation of grains is not taken into account; they cannot be used in the macroscopic theories. The average over the sample \bar{c} has clear physical sense.

We suggest the following ways to present a multivariant structure in the polycrystal. For local presentation, one can show a triad of local crystallographic axes in each grain along with fields c_i (Fig. 1a). One can present fields of six components of $\varepsilon_{ii}c_i$ for each variant M_i in the global coordinate system, which is 18 fields. For the above example with 5 grains, in each grain, we will have components of ε_{i3} in the global coordinate system, which is consistent with the treatment of the aggregate as a single crystal. More compact is to present six fields of six components of the total transformation strain $\varepsilon_i = \sum_{i=1}^m \varepsilon_{ii}c_i$ in the global coordinate system (Figs. 4 and 5), which takes into account in more averaged sense both an orientation of grain and fields c_i . For the averaged description, one can use a plot of six components of $\bar{\varepsilon}_t$.

As it follows from Figs. 4 and 5, normal components of ε_t vary between extremes -0.447 and 0.1753 corresponding to the full local transformation in single variant oriented along the global coordinate axes, despite zero averaged total lateral strains. Shear components vary between extremes ± 0.31 , also despite zero averaged. Colors corresponding to zero value of each component of transformation strain is clear from colors of large Si I regions at 25% transformation progress corresponding c=0 in Figs. 2 and 3. For both grain sizes one sees strong heterogeneity of transformation strains from grain to grain and within grains. Note that fields at the surface do not completely represent fields in the entire volume, that is why some results may look counterintuitive. For example, while averaged ε_t^{33} is larger than ε_t^{11} and ε_t^{22} , this is not evident from the surface fields.

Despite the fact that for the smaller number of grains size of Si II units is larger, difference in $\bar{c}(\bar{E}_{33})$ (and even $\bar{c}_i(\bar{E}_{33})$) for different number of grains is small (Fig. 6). Initiation of PT occurs at the same

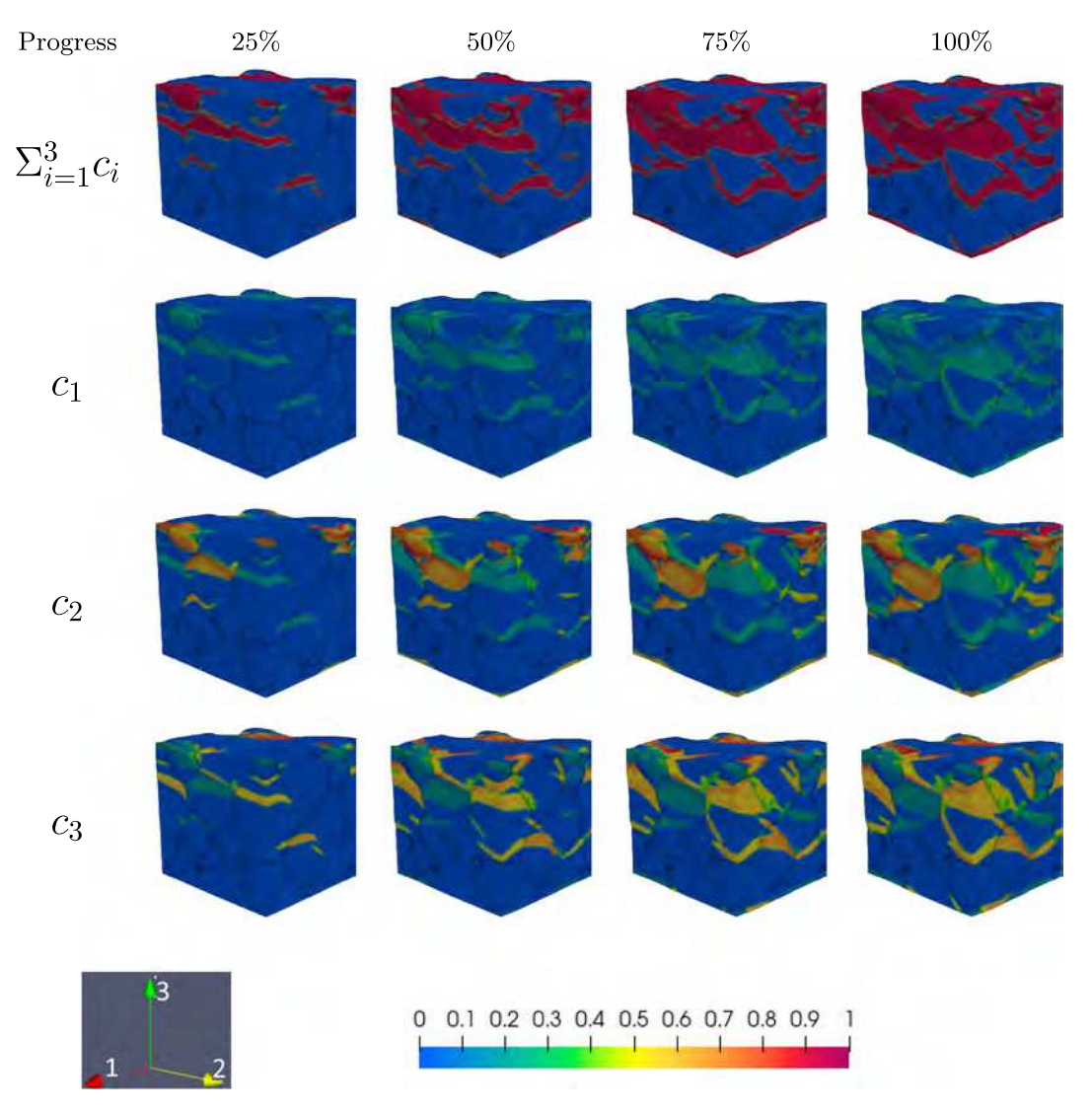


Fig. 14. Evolution of volume fractions of phases for stress-controlled loading of a sample with 55 grains.

stress $\sigma_{zz} = -10.33$ GPa for both grain sizes, and stress-strain curves in Fig. 9 also differ insignificantly. That means that the current model does not describe experimentally observed effect of the grain size on the Si I to Si II PT pressure or stress [24,62-64]. This is not surprising and expected for any scale-free model, especially for a change in grain size as small as by a factor of 2.5. The main classical reason for a scale effect is a limited number of nucleation sites in small grains [65]. Since the current model does not include dislocations as local stress concentrators in bulk and at grain boundaries, it should not exhibit any grain size effect. This will be the next step in the development of this model. We plan to apply the same scale-free approach for introducing discrete dislocations via the solution of the contact problem, as it was done in [66,67] for small strains and 2D formulations. Of course, it is much more challenging to do this for 3D and large strains. Another reason for grain-size dependence of PT parameters for grain sizes less than 100 nm is the finite width (~1 nm) of a disordered grain boundary in 1D model in [68]. Some nanoscale PFAs also introduced the finite width of the grain boundaries, also ~1 nm thick, to either fully suppress PT in it [69,70] or, in contrast, promote nucleation by relaxing transformation strain in the grain boundaries [71,72]. While both types of advancements of the PFA reach clear qualitative goals, the reality is much more complex. These works neglect misorientation angle between grains, while even our simplest model with zero-width grain boundaries shows that for small misorientations, transfer of PT

from grain to grain easily occurs, while for large misorientations it does not. Changes in grain boundary energy during PT and surface stresses at phase interfaces and grain boundaries may play a crucial role in promoting or suppressing nucleation at the grain boundary, similar to an external surface [73]. Also, the ratio of the width of grain boundary to the phase interface width may strongly affect solutions [74,75]. However, all these nanoscale effects cannot be included in a scale-free model applicable to large samples.

Figs. 7 and 8 shows the evolution of all components of Cauchy stresses throughout the simulation. It can be noticed from Figs. 7 and 8 that the grain boundaries and triple junctions have the highest stresses of both signs, which cause nucleation of the dominating variant accompanied by two other variants and growth, often along the grain boundaries. Next, a large stress concentration of both signs appears at the phase interface, causing further nucleation in bulk (so-called autocatalytic effect). The peak stresses are huge for both normal and even shear stresses. Thus, for small grains, σ_{22} varies from -45 to 35 GPa and σ_{33} varies from -40 to 10 GPa. Similar, shear stress σ_{12} varies from -20 to 20 GPa and σ_{23} varies from -15 to 15 GPa. For large grains, the magnitude of extremes in stresses is smaller by 5 to 10 GPa. Despite this difference for different grain sizes, the macroscopic PT initiation stress $\sigma_{zz} = -10.33$ GPa is the same, and the entire $\sigma_{zz} - \varepsilon_{zz}$ curve do not differ significantly. The initiation stress is determined by the transformation work, which depends on all components of the stress

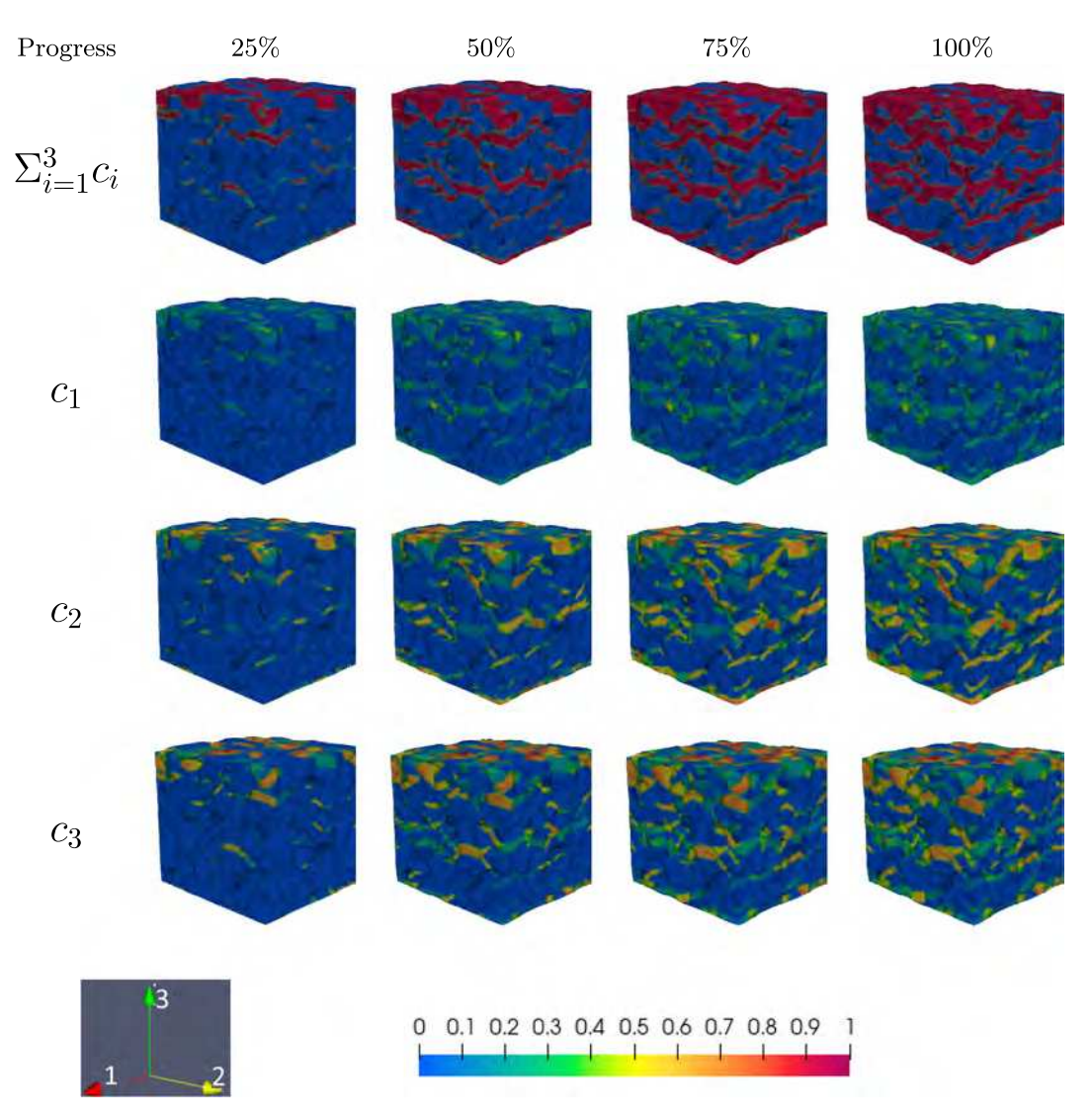


Fig. 15. Evolution of volume fractions of phases for stress-controlled loading of a sample with 910 grains.

tensor. While stresses are different, the transformation work may be approximately the same for both grain sizes. This is similar to results in [40], where a strong stress concentrator due to a dislocation in Si produced a relatively small contribution to the transformation work.

The stress-strain plots for strain-controlled loading are given in Fig. 9. After PT starts at $\bar{E}_{33} = -0.06$ and $\bar{\sigma}_{33} = -10.33$ GPa for both small and large grains, the stress-strain plots continue along the elastic curve of the austenite with small nonlinearities. This behavior is because, initially, the transformation rate is very low, as can be noticed from Fig. 6. Si II nuclei are localized near stress concentrators without essential growth. Only at $\bar{E}_{33} = -0.07$ does intense growth start, which leads to a strong reduction in tangent modulus. Note that for a single crystal, the tangent modulus is getting negative at the onset of the PT, causing macroscopic instability [47]. In contrast, for polycrystals, the local mechanical instabilities due to PT and negative local tangent modulus are stabilized at the macroscale by arresting/slowing the growth of Si II regions by the grain boundaries and generating the internal back stresses. This is reflected by the positive tangent moduli in the stress-strain plots in Fig. 9. While intuitively, the more grain boundaries we have, the higher the tangent moduli should be, in fact, the response for 910 grains is slightly softer than that of 55 grains Fig. 9. The reasons are: (a) more triple junctions and nucleation sites for smaller grains leading to more Si II regions; (b) smaller misorientation between neighboring grains leading to easier transfer of PT growth

from grain to grain, and (c) a larger number of surrounding grains giving more chances to find proper orientation for new nucleation caused by internal stresses in the transforming grains. Although there is a noticeable difference in the response for both cases, the maximum difference is <1 GPa or <10%. Such a small difference implies that it is unnecessary to treat a sample with such a large number of grains to estimate the macroscopic behavior of a polycrystal. Note that the Lagrangian elastic strain at the end of simulation, at $\bar{E}_{33}=-0.22$, is -0.1, i.e., comparable to the transformation strain.

Figs. 10 and 11 shows the pole figures for 55 and 910 grains, respectively. Figs. 10(a) and 11(a) for initial austenite demonstrate quite an even spread in all the directions because the random texture of the stress-free initial configuration was chosen. Fig. 10(a) shows few low-density regions because of the lower number of grains. Comparing the initial (Fig. 10(a)) and final (Fig. 10(b)) austenite for 55 grains, we can clearly notice depletion of the austenite grains due to their transformation to martensite. Similar depletion is not noticed in Fig. 11(b) for 910 grains because many grains do not completely transform to martensite. The increase in density in Figs. 10(b) or 11(b) is because of the rotation of part of or entire austenitic grains, which was observed for single crystal as well [47].

Figs. 10(c)–(e) and 11(c)–(e) present the pole figures for the three martensitic variants at the last stage of simulations. As expected, there is a 90° rotation relation between the first and the second or the third

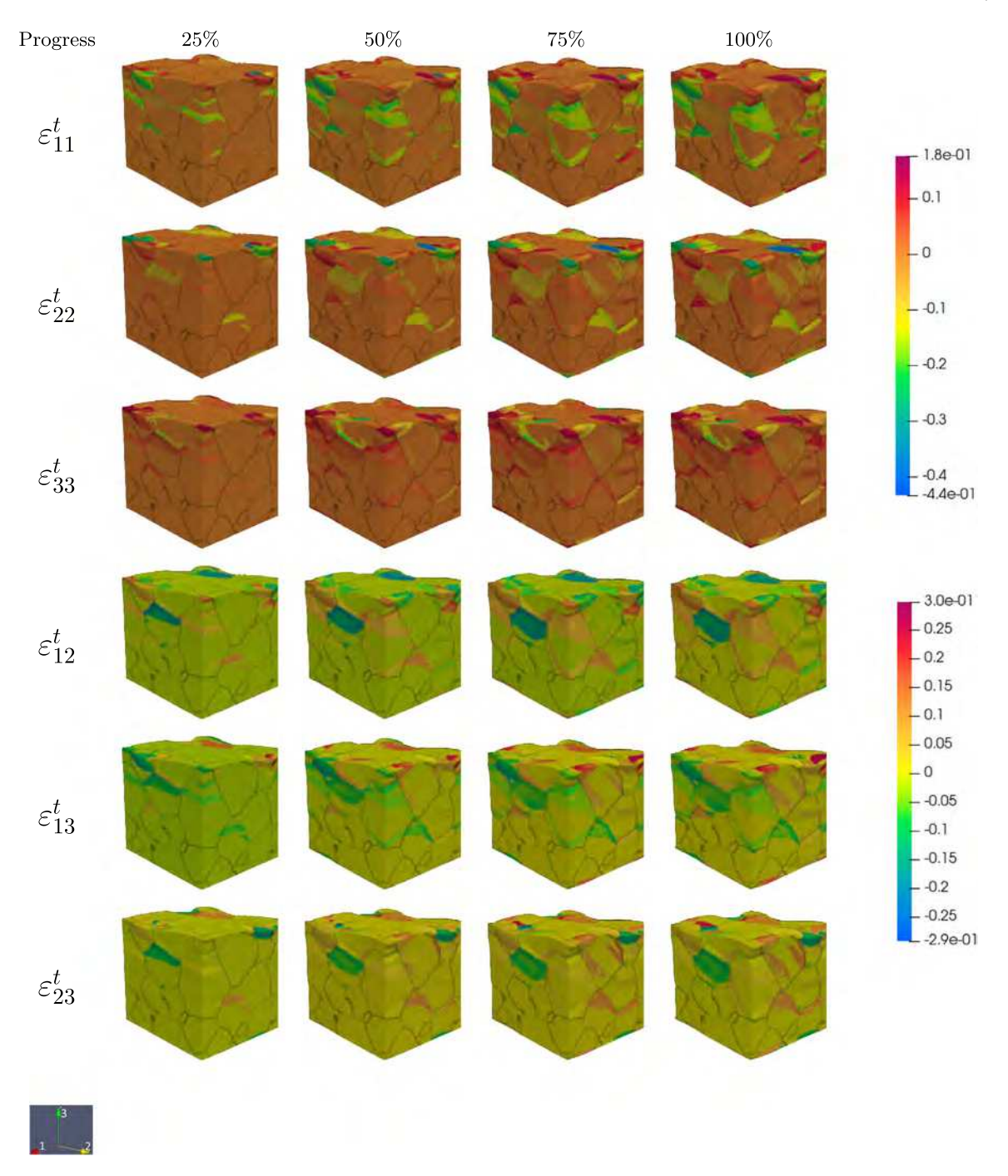


Fig. 16. Evolution of the components of the transformation strain tensor for stress-controlled loading of a sample with 55 grains.

variant about the (001) axis. The trends in the volume fractions of the individual martensitic variant in Figs. 10 and 11 match that of Fig. 6. The first variant is the lowest in both cases, as only the grains that have their c-axis aligned with the loading direction can transform to the first variant. As for the second or the third variants, they primarily need to be oriented such that their a or b-axis needs to be aligned with the loading direction. But because of the boundary conditions used, there are lateral stresses which can contribute to giving a resultant load in the preferred axes assisting in the transformation. This phenomenon is not possible for the first variant as the lateral stresses are only a fraction of the applied load and cannot be the primary contributor to fulfilling the phase transformation criteria.

4.3. Stress-controlled loading

In stress-controlled, the stress is applied at a rate of -4 MPa/s till it reaches -11 GPa and held constant thereafter. Figs. 14 and 15 show the evolution of the volume fraction of Si II and the individual martensitic variants, Figs. 16 and 17 show the transformation strain tensor components, and Figs. 18 and 19 show the stress components at different simulation stages for 55 and 910 grains. The videos showing the evolution of the volume fractions are provided in the supplementary material. Volume fraction of each martensitic variant \bar{c}_i averaged over the sample based on Eq. (17) and \bar{c} vs. strain is shown in Fig. 13. There is no significant difference, in comparison with the strain-controlled

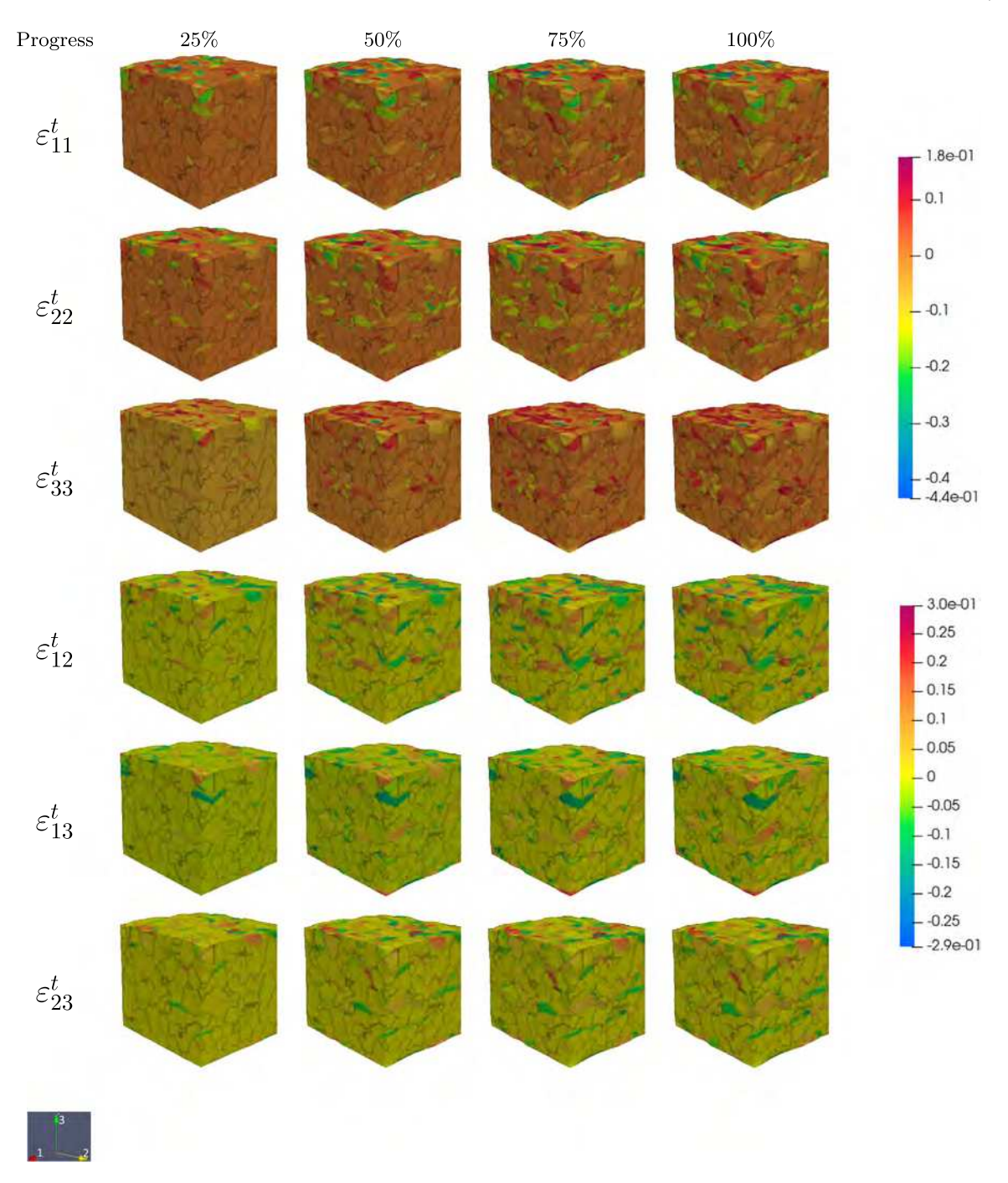


Fig. 17. Evolution of the components of the transformation strain tensor for strain-controlled loading of a sample with 910 grains.

case, in nucleation at grain boundaries and triple junctions and character of growth of martensitic units, stress concentrations, and that $\bar{c}_2 \simeq \bar{c}_3 \simeq 2\bar{c}_1$. The same discussion on the luck of the physical sense in \bar{c}_i is valid; \bar{c} has a physical meaning only.

Stress-controlled compression for both numbers of grains is up to 42% transformation to Si II, after which process diverges. The stress-strain plots for strain-controlled loading are given in Fig. 12. The PT starts immediately at -11 GPa and continues to the end of simulations at $E_{33}=-0.116$. These values are larger than those for strain-controlled loading: at -11 GPa, we have $E_{33}=-0.063$ and $c=2.4\times10^{-3}$ only; however, at $E_{33}=-0.116$ one gets c=0.362 for strain-controlled loading. The possibility of larger strains and transformation progress

at -11 GPa is related to less constraint deformation at the horizontal external surfaces. Periodic conditions for displacements along the axis 3 for strain-controlled loading lead to more homogeneous PT near both horizontal surfaces and small deviations from the flat surfaces. In contrast, for stress-controlled loading, lack of periodic conditions along the axis 3 leads to much pronounced PT near the upper horizontal surface, which spreads in the upper part of the sample. This leads to the loss of stability of Si II nuclei near stress concentrators, their fast growth, interaction, coalescence, and more pronounced auto-catalytic effect. Thus, specific boundary conditions are very influential, which is necessary to take into account in the problem formulation. The difference in volume fractions of M_i for 55 and 910 grains in Fig. 6

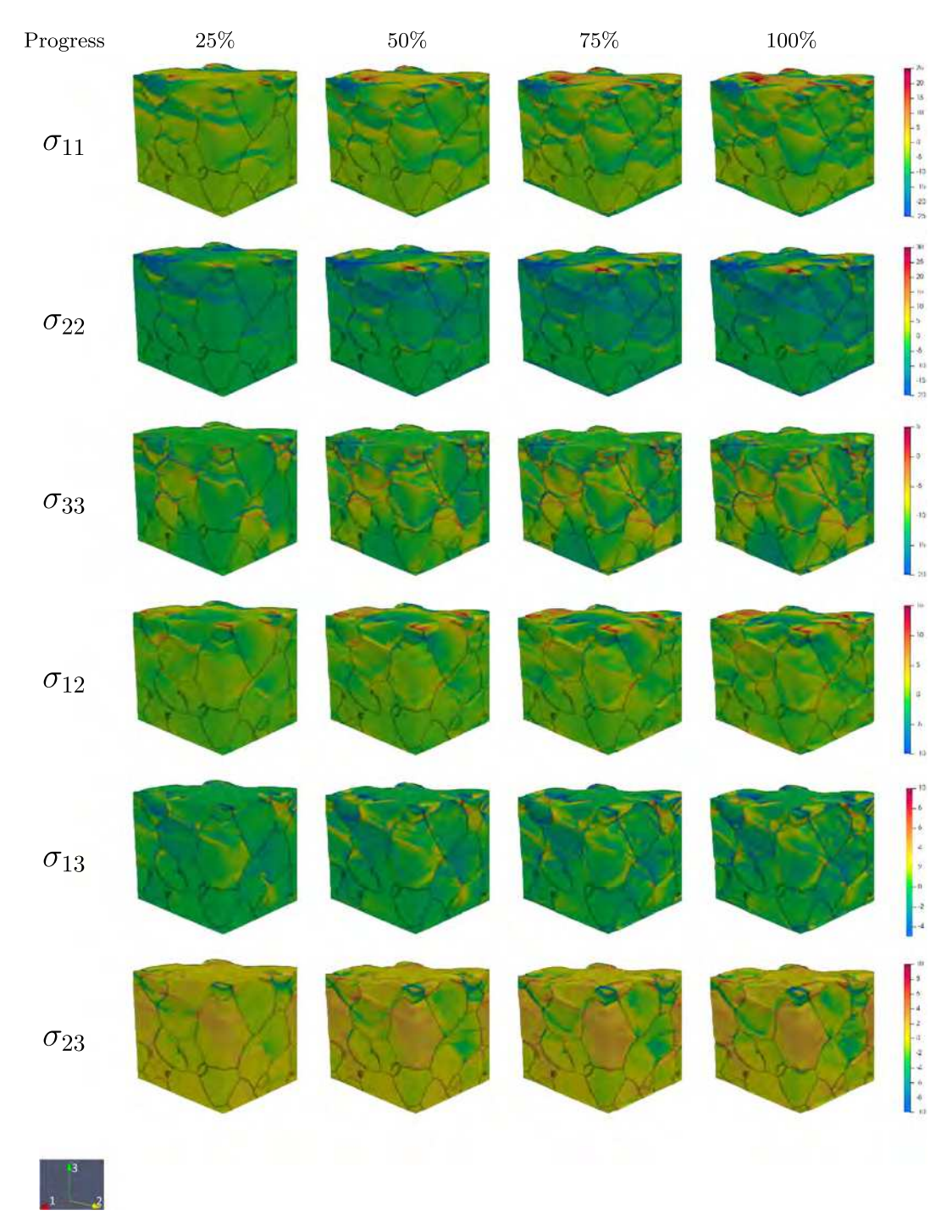


Fig. 18. Evolution of the components of the Cauchy stress tensor for stress-controlled loading of a sample with 55 grains.

and \bar{c} is much smaller than for the strain-controlled loading in Fig. 6, again due to less restrictive boundary conditions.

The peak stresses are large but smaller than for strain-controlled loading (Figs. 18 and 19). Thus, for small grains, σ_{22} varies from -33 to 30 GPa and σ_{33} varies from -25 to 5 GPa. Similar, shear stress σ_{12} and σ_{23} vary from -15 to 15 GPa. For large grains, the magnitude of extremes in stresses are smaller by 5 to 10 GPa, like for strain-controlled loading. Lower peak stresses are partially caused by a smaller volume fraction of Si II.

Figs. 20 and 21 show the pole figures for 55 and 910 grains, respectively, for the stress-controlled loading. Figs. 20(a) and 21(a) show initial austenite texture for both cases, which are the same as

the ones chosen for strain-controlled loading. For both 55 and 910 grains, there is no significant depletion of the austenite, unlike for the strain-controlled loading, because the $\bar{c}=0.42$ only. This is reflected in the small difference between Fig. 20(a) and (b), and in sparsely distributed Fig. 20(c)–(e). Contrary to this, Fig. 21(c)–(e) show the pole figures with more uniform distributions because grains in many different orientations start transforming to martensite like in the case of Fig. 11.

5. Concluding remarks

In the paper, the first scale-free PFA modeling of the multivariant martensitic PT from cubic Si I to tetragonal Si II in a polycrystalline

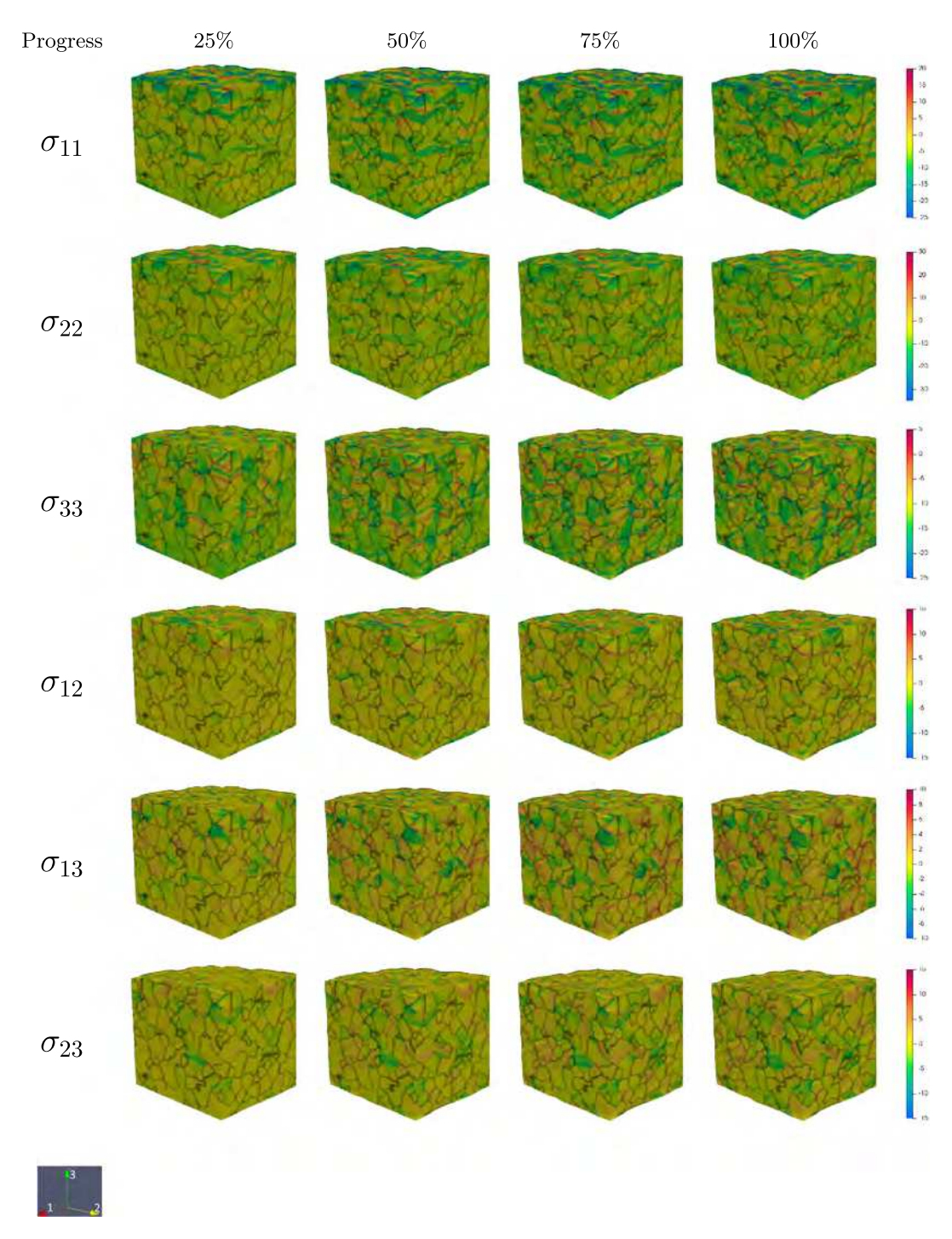


Fig. 19. Evolution of the components of the Cauchy stress tensor for strain-controlled loading of a sample with 910 grains.

aggregate with up to 1000 grains is presented. All computational challenges related to large and very anisotropic transformation strain tensors, the stress-tensor dependent athermal dissipative threshold for the PT, and elastic instabilities due to a variety of complex loadings in each grain, are overcome. The importance of the simulations should also be stressed by the fact that since Si II does not exist under ambient conditions, its microstructure cannot be studied using traditional postmortem methods (SEM, TEM, etc.). For a single crystal, positions of Si I-Si II interfaces can be determined using in-situ high-pressure Laue diffraction, but still, in combination with molecular dynamics [37]. For polycrystals, this is currently impossible.

Coupled evolution of discrete martensitic microstructure, volume fractions of martensitic variants, and Si II, stress and transformation strain tensors, and texture are presented and analyzed. It is demonstrated that the volume fraction of each martensitic variant c_i in each grain does not have a lot of sense unless the orientation of the grain is explicitly shown. The average over the sample \bar{c}_i does not have any physical sense because the orientation of grains is not taken into account; they are misleading and cannot be used in the macroscopic theories. Macroscopic variables effectively representing multivariant transformational behavior are introduced. One can present fields of six components of $\varepsilon_{ii}c_i$ for each variant M_i in the global coordinate system.

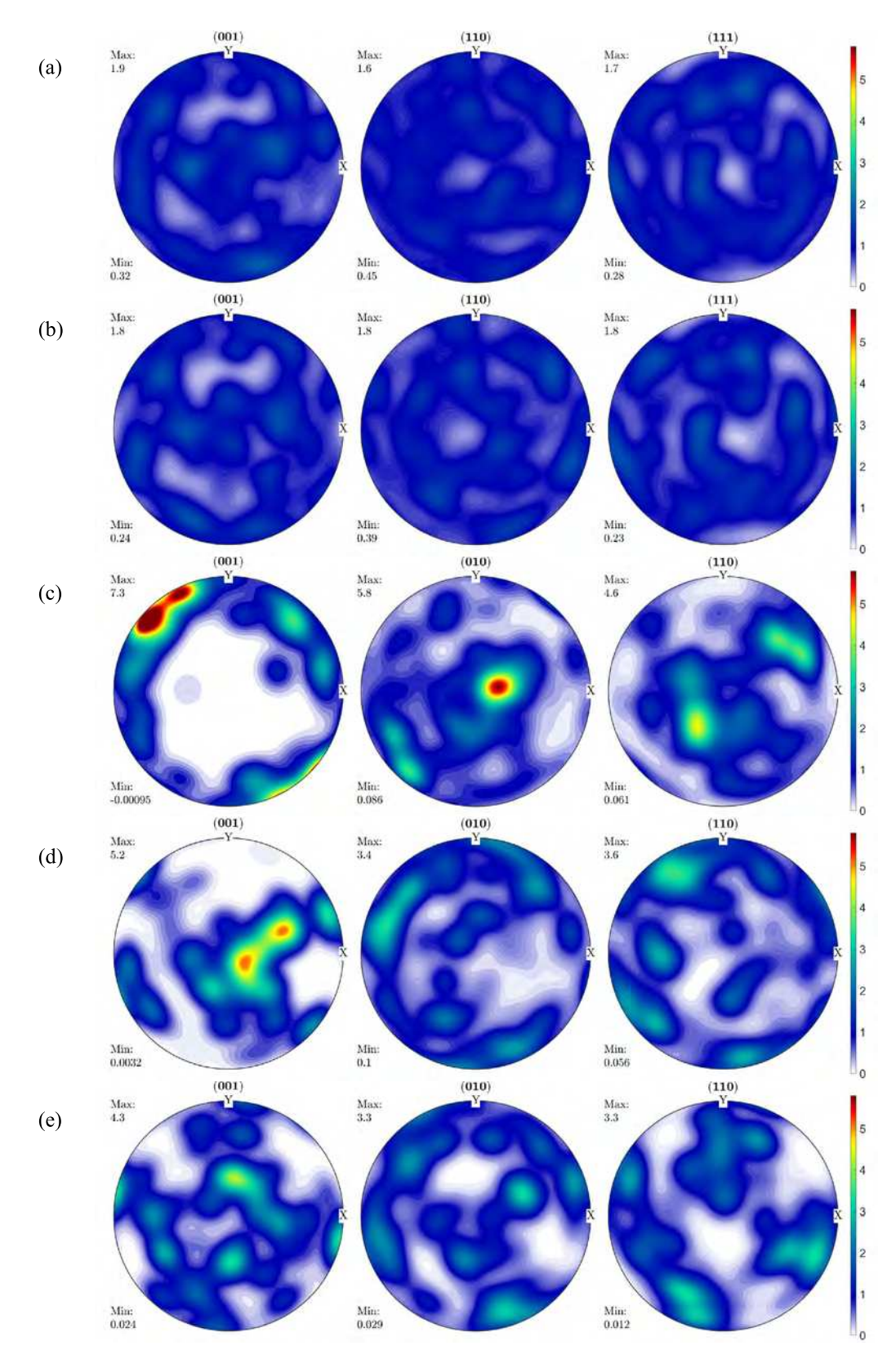


Fig. 20. Pole figures of (a) initial austenite, (b) residual austenite, (c) final martensitic variant M_1 , (d) M_2 , and (e) M_3 for stress-controlled loading of 55 grains.

More compact is to present six components of the total transformation strain $\epsilon_t = \sum_{i=1}^m \epsilon_{ti} c_i$ in the global coordinate system. For the averaged description, one can utilize six components of $\bar{\epsilon}_t$.

For strain-controlled uniaxial compression with periodic conditions in all directions, almost complete (96%) PT was reached with small

pockets of residual Si I. For stress-controlled uniaxial compression without periodic conditions in the loading direction, 42% of completion of was achieved at -11 GPa, much larger than 0.24% for the same axial stress for strain-controlled loading, but relatively close volume fraction of Si II was reached for the same strain. Lack of periodic

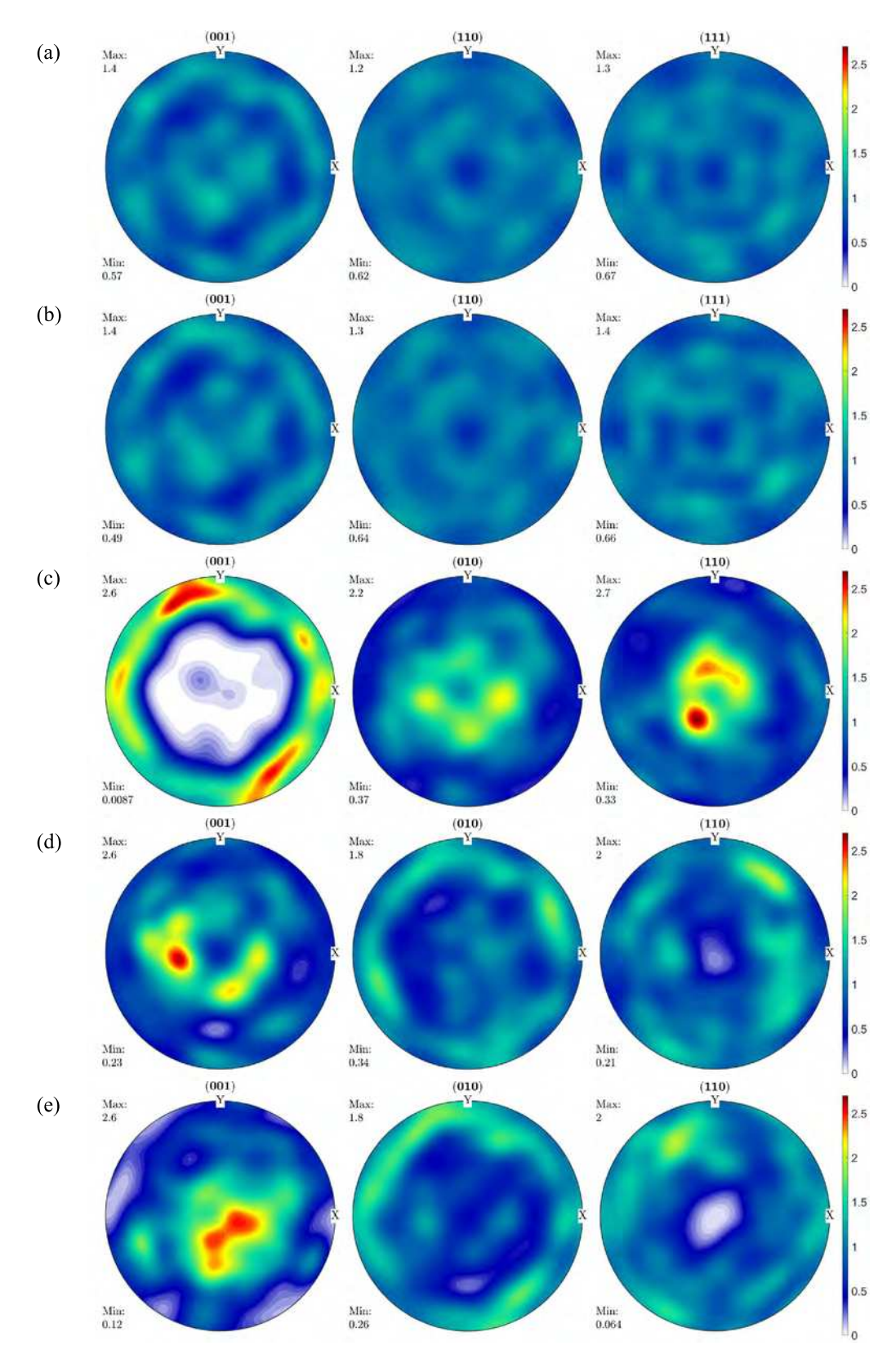


Fig. 21. Pole figures of (a) initial austenite, (b) residual austenite, (c) final martensitic variant M_1 , (d) M_2 , and (e) M_3 for stress-controlled loading of 910 grains.

conditions in the loading direction results in less constraint deformation at the horizontal external surfaces and more localized transformation near one of them, which leads to loss of stability of Si II nuclei near

stress concentrators, their fast growth, interaction, and coalescence. Thus, tiny detail in the boundary conditions is very influential, which is necessary to take into account in the problem formulation.

Despite the simplest model for the grain boundaries, namely zero width 2D surfaces with a jump of all orientation-dependent material properties, they reproduce the main desired features generically observed in experiments and nanoscale PFAs with finite-width grain boundaries [69–72] for various material systems. The general trend is that the lower-angle grain boundaries produce lower stress concentration for martensite nucleation but lower resistance for martensitic units to pass from grain to grain. The larger-angle grain boundaries produce large stress concentration and cause nucleation and growth of martensite along the grain boundary but strongly resist or prevent passing PT to the neighboring grain. Note that models [69–72] do not include misorientation of grains in the grain boundary model and athermal interfacial friction, in contrast to our model.

In contrast to a single crystal, the local mechanical instabilities due to PT and negative local tangent modulus are stabilized at the macroscale by arresting/slowing the growth of Si II regions by the grain boundaries and generating the internal back stresses. This leads to an increasing magnitude of stress during PT, typical for various nonhydrostatic loadings of Si in experiments [15,24]. Of course, a more realistic model of the grain boundaries is required, but it is not clear how properties of a nanometer thick grain boundary can be effectively included in a model for large samples.

Large transformation strains and grain boundaries lead to huge internal stresses, which affect the microstructure evolution and macroscopic behavior. The peak stresses reach 45 GPa in compression, 35 GPa in tension, and 20 GPa in shear for strain-controlled loading of 910 grains; for 55 grains, the magnitude of extremes in stresses are smaller by 5 to 10 GPa. For stress-controlled loading and small grains, the peak stresses reach 35 GPa in compression, 30 GPa in tension, and 15 GPa in shear; for large grains, they are smaller by 5-10 GPa, like for strain-controlled loading. Lower peak stresses for stress-controlled loading are partially caused by a smaller volume fraction of Si II. Despite these differences, the macroscopic (overall) stress-strain and transformational behavior for 55 and 910 grains are quite close and differ less than by 10% for strain-controlled loading and even less for stress-controlled one. This allows the determination of the macroscopic constitutive equations by treating aggregate with a small number of grains. On the other hand, that means that the current model does not describe experimentally observed effect of the grain size on the Si I to Si II PT pressure or stress [24,62-64]; however, this is not surprising and was expected for any scale-free model. The reason is that the current model does not include dislocations as local stress concentrators in bulk and at grain boundaries. This will be the next step in developing the current model. We can use the same approach for introducing discrete dislocations via the solution of the contact problem, as it was done in [66,67] for small strains and 2D formulations.

Obtained results are also an important step in studying plastic strain-induced PTs. The main hypothesis [12] is that they initiate at the tip of dislocation pileups against grain boundaries, which causes strong stress concentration for all stress components proportional to the number of dislocations in a pileup. These stresses drastically reduce the required external pressure needed for nucleation and further growth. Nanoscale PFA for coupled PTs and discrete dislocations allows us to treat a bicrystal and to qualitatively prove this hypothesis [76–78], however, for 2D and small strain formulation. Our scale-free PFA [66,67] introduced discrete dislocations via the solution of the contact problem. It has been applied to 2D polycrystalline samples with several dozen grains and also for small strain formulation. Of course, it is much more challenging to do this for 3D and large strains.

In [56,69,70], continuum von Mises plasticity is included in PFAs for PTs. While this is a reasonably good way to describe stress relaxation for temperature-, pressure-, and stress-induced PTs, description of plastic strain-induced PTs requires discrete dislocation microstructure and corresponding stress concentrators.

The developed methodology can be used for studying various PTs with large transformation strains (e.g., hexagonal and rhombohedral graphite to hexagonal and cubic diamond, similar PTs from graphite-like BN to superhard diamond-like BN, PTs in semiconducting Ge and GaSb, etc.) and for further development for plastic strain-induced PTs. Elastic instabilities with the problems discussed in Section 4.1 are expected for these crystals as well, thus strict methods of their inclusion in the PT kinetics should be developed.

Declaration of competing interest

The authors declare that they have no known competing financial interests or personal relationships that could have appeared to influence the work reported in this paper.

Acknowledgments

The support of National Science Foundation (CMMI-1943710 and MMN-2246991) and Iowa State University (Vance Coffman Faculty Chair Professorship) is gratefully acknowledged. The simulations were performed at Extreme Science and Engineering Discovery Environment (XSEDE), allocation TG-MSS170015.

Appendix A. Supplementary data

Supplementary material related to this article can be found online at https://doi.org/10.1016/j.actamat.2023.118996.

References

- [1] G.A. Heath, T.J. Silverman, M. Kempe, M. Deceglie, D. Ravikumar, T. Remo, H. Cui, P. Sinha, C. Libby, S. Shaw, et al., Research and development priorities for silicon photovoltaic module recycling to support a circular economy, Nat. Energy 5 (7) (2020) 502–510.
- [2] J. Chelikowsky, Introduction: Silicon in all its forms, in: P. Siffert, E.F. Krimmel (Eds.), Silicon: Evolution and Future of a Technology, Springer Berlin Heidelberg, Berlin, Heidelberg, ISBN: 978-3-662-09897-4, 2004, pp. 1–22.
- [3] V. Domnich, D. Ge, Y. Gogotsi, Indentation-induced phase transformations in semiconductors, in: V. Domnich, Y. Gogotsi (Eds.), High Pressure Surface Science and Engineering; Section 5.1, Institute of Physics, Bristol, 2004, pp. 381–442.
- [4] M.S. Kiran, B. Haberl, J.E. Bradby, J.S. Williams, Chapter Five Nanoindentation of Silicon and Germanium, in: L. Romano, V. Privitera, C. Jagadish (Eds.), Defects in Semiconductors, in: Semiconductors and Semimetals, vol. 91, Elsevier, (ISSN: 0080-8784) 2015, pp. 165–203, http://dx.doi.org/10.1016/bs.semsem.2014.12.
- [5] S. Goel, X. Luo, A. Agrawal, R.L. Reuben, Diamond machining of silicon: a review of advances in molecular dynamics simulation, Int. J. Mach. Tools Manuf. 88 (2015) 131–164.
- [6] Y. Ikoma, K. Hayano, K. Edalati, K. Saito, Q. Guo, Z. Horita, Phase transformation and nanograin refinement of silicon by processing through high-pressure torsion, Appl. Phys. Lett. 101 (12) (2012) 121908.
- [7] Y. Ikoma, K. Hayano, K. Edalati, K. Saito, Q. Guo, Z. Horita, T. Aoki, D.J. Smith, Fabrication of nanograined silicon by high-pressure torsion, J. Mater. Sci. 49 (2014) 6565–6569.
- [8] J.A. Patten, H. Cherukuri, J. Yan, Ductile-regime machining of semiconductors and ceramics, in: V. Domnich, Y. Gogotsi (Eds.), High-Pressure Surface Science and Engineering, Institute of Physics, Bristol, 2004, pp. 543–632.
- [9] Z. Malyushitskaya, Mechanisms responsible for the strain-induced formation of metastable high-pressure Si, Ge, and GaSb phases with distorted tetrahedral coordination, Inorg. Mater. 35 (5) (1999) 425–430.
- [10] V.I. Levitas, H. Chen, L. Xiong, Lattice instability during phase transformations under multiaxial stress: Modified transformation work criterion, Phys. Rev. B 96 (2017) 054118, http://dx.doi.org/10.1103/PhysRevB.96.054118.
- [11] V.I. Levitas, H. Chen, L. Xiong, Triaxial-Stress-Induced Homogeneous Hysteresis-Free First-Order Phase Transformations with Stable Intermediate Phases, Phys. Rev. Lett. 118 (2017) 025701, http://dx.doi.org/10.1103/PhysRevLett.118. 025701.
- [12] V.I. Levitas, High-pressure mechanochemistry: Conceptual multiscale theory and interpretation of experiments, Phys. Rev. B 70 (2004) 184118, http://dx.doi.org/ 10.1103/PhysRevB.70.184118.
- [13] V.I. Levitas, High pressure phase transformations revisited, J. Phys.: Condens. Matter 30 (16) (2018) 163001, http://dx.doi.org/10.1088/1361-648X/aab4b0.

[14] V.I. Levitas, High-pressure phase transformations under severe plastic deformation by torsion in rotational anvils, Mater. Trans. 60 (7) (2019) 1294–1301.

- [15] V.D. Blank, E.I. Estrin, Phase Transitions in Solids under High Pressure, CRC Press. 2013.
- [16] P.W. Bridgman, Effects of High Shearing Stress Combined with High Hydrostatic Pressure, Phys. Rev. 48 (1935) 825–847, http://dx.doi.org/10.1103/PhysRev.48. 825.
- [17] K. Edalati, Z. Horita, A review on high-pressure torsion (HPT) from 1935 to 1988, Mater. Sci. Eng. A (ISSN: 0921-5093) 652 (2016) 325–352, http://dx.doi. org/10.1016/j.msea.2015.11.074.
- [18] Y. Gao, Y. Ma, Q. An, V. Levitas, Y. Zhang, B. Feng, J. Chaudhuri, W.A. Goddard, Shear driven formation of nano-diamonds at sub-gigapascals and 300 K, Carbon (ISSN: 0008-6223) 146 (2019) 364–368, http://dx.doi.org/10.1016/j.carbon.2019.02.012.
- [19] V.I. Levitas, L.K. Shvedov, Low-pressure phase transformation from rhombohedral to cubic BN: Experiment and theory, Phys. Rev. B 65 (2002) 104109, http: //dx.doi.org/10.1103/PhysRevB.65.104109.
- [20] C. Ji, V.I. Levitas, H. Zhu, J. Chaudhuri, A. Marathe, Y. Ma, Shear-induced phase transition of nanocrystalline hexagonal boron nitride to wurtzitic structure at room temperature and lower pressure, Proc. Natl. Acad. Sci. 109 (47) (2012) 19108–19112.
- [21] K. Pandey, V.I. Levitas, In situ quantitative study of plastic strain-induced phase transformations under high pressure: Example for ultra-pure Zr, Acta Mater. (ISSN: 1359-6454) 196 (2020) 338–346, http://dx.doi.org/10.1016/j.actamat. 2020.06.015.
- [22] V. Levitas, F. Lin, K. Pandey, S. Yesudhas, C. Park, Laws of high-pressure phase and nanostructure evolution and severe plastic flow, September 9, Res. Sq. (2022) 29, http://dx.doi.org/10.21203/rs.3.rs-1998605/v1.
- [23] M. Aleksandrova, V. Blank, S. Buga, Phase transitions in Ge and Si under shear deformation at pressure up to 12 GPa conditions and P-T- gamma[shear] diagrams of these elements, Phys. Solid State 35 (5) (1993) 1308–1317.
- [24] S. Yesudhas, V.I. Levitas, F. Lin, K.K. Pandey, J. Smith, Plastic strain-induced phase transformations in silicon: drastic reduction of transformation pressures, change in transformation sequence, and particle size effect, 2023, arXiv:2303. 04407.
- [25] G. Voronin, C. Pantea, T. Zerda, L. Wang, Y. Zhao, In situ x-ray diffraction study of silicon at pressures up to 15.5 GPa and temperatures up to 1073 K, Phys. Rev. B 68 (2) (2003) 020102.
- [26] J. Pokluda, M. Černý, M. Šob, Y. Umeno, Ab initio calculations of mechanical properties: Methods and applications, Prog. Mater. Sci. 73 (2015) 127–158.
- [27] Y. Umeno, M. Černỳ, Effect of normal stress on the ideal shear strength in covalent crystals, Phys. Rev. B 77 (10) (2008) 100101.
- [28] R. Telyatnik, A. Osipov, S. Kukushkin, Ab initio modelling of nonlinear elastoplastic properties of diamond-like C, SiC, Si, Ge crystals upon large strains., Mater. Phys. Mech. 29 (1) (2016) 1–16.
- [29] M. Černý, P. Řehák, Y. Umeno, J. Pokluda, Stability and strength of covalent crystals under uniaxial and triaxial loading from first principles, J. Phys.: Condens. Matter 25 (3) (2012) 035401.
- [30] N.A. Zarkevich, H. Chen, V.I. Levitas, D.D. Johnson, Lattice instability during solid-solid structural transformations under a general applied stress tensor: Example of Si I → Si II with metallization, Phys. Rev. Lett. 121 (16) (2018) 165701.
- [31] H. Chen, N.A. Zarkevich, V.I. Levitas, D.D. Johnson, X. Zhang, Fifth-degree elastic energy for predictive continuum stress-strain relations and elastic instabilities under large strain and complex loading in silicon, NPJ Comput. Mater. 6 (1) (2020) 115.
- [32] V.I. Levitas, Phase-field theory for martensitic phase transformations at large strains, Int. J. Plast. 49 (2013) 85–118.
- [33] P. Valentini, W.W. Gerberich, T. Dumitrică, Phase-Transition Plasticity Response in Uniaxially Compressed Silicon Nanospheres, Phys. Rev. Lett. 99 (2007) 175701, http://dx.doi.org/10.1103/PhysRevLett.99.175701.
- [34] D. Chrobak, N. Tymiak, A. Beaber, O. Ugurlu, W.W. Gerberich, R. Nowak, Deconfinement leads to changes in the nanoscale plasticity of silicon, Nature Nanotechnol. 6 (8) (2011) 480–484.
- [35] H. Chen, V.I. Levitas, L. Xiong, Amorphization induced by 60° shuffle dislocation pileup against different grain boundaries in silicon bicrystal under shear, Acta Mater. 179 (2019) 287–295.
- [36] L.C. Zhang, W.C.D. Cheong, Molecular dynamics simulation of phase transformations in monocrystalline silicon, in: V. Domnich, Y. Gogotsi (Eds.), High Pressure Surface Science and Engineering, Institute of Physics, Bristol, 2004, pp. 57–119.
- [37] H. Chen, V.I. Levitas, D. Popov, N. Velisavljevic, Nontrivial nanostructure, stress relaxation mechanisms, and crystallography for pressure-induced Si-I → Si-II phase transformation, Nature Commun. (ISSN: 20411723) 13 (1) (2022) 982, http://dx.doi.org/10.1038/S41467-022-28604-1.
- [38] V.I. Levitas, Phase field approach for stress- and temperature-induced phase transformations that satisfies lattice instability conditions. Part I. General theory, Int. J. Plast. (ISSN: 0749-6419) 106 (2018) 164–185, http://dx.doi.org/10.1016/ J.IJPLAS.2018.03.007.

[39] H. Babaei, V.I. Levitas, Phase-field approach for stress- and temperature-induced phase transformations that satisfies lattice instability conditions. Part 2. Simulations of phase transformations Si I → Si II, Int. J. Plast. 107 (2018) 223–245, http://dx.doi.org/10.1016/j.iiplas.2018.04.006.

- [40] H. Babaei, V.I. Levitas, Effect of 60° dislocation on transformation stresses, nucleation, and growth for phase transformations between silicon I and silicon II under triaxial loading: Phase-field study, Acta Mater. 177 (2019) 178–186.
- [41] H. Babaei, V.I. Levitas, Stress-Measure Dependence of Phase Transformation Criterion under Finite Strains: Hierarchy of Crystal Lattice Instabilities for Homogeneous and Heterogeneous Transformations, Phys. Rev. Lett. 124 (2020) 075701, http://dx.doi.org/10.1103/PhysRevLett.124.075701.
- [42] H. Babaei, A. Basak, V.I. Levitas, Algorithmic aspects and finite element solutions for advanced phase field approach to martensitic phase transformation under large strains, Comput. Mech. (ISSN: 14320924) 64 (4) (2019) 1177–1197, http://dx.doi.org/10.1007/S00466-019-01699-Y.
- [43] V.I. Levitas, M. Javanbakht, Phase-field approach to martensitic phase transformations: Effect of martensite-martensite interface energy, Int. J. Mater. Res. (ISSN: 18625282) 102 (6) (2011) 652-665, http://dx.doi.org/10.3139/146.
- [44] V.I. Levitas, A.V. Idesman, D.L. Preston, Microscale simulation of martensitic microstructure evolution, Phys. Rev. Lett. 93 (10) (2004) 105701.
- [45] A.V. Idesman, V.I. Levitas, D.L. Preston, J.-Y. Cho, Finite element simulations of martensitic phase transitions and microstructures based on a strain softening model, J. Mech. Phys. Solids 53 (3) (2005) 495–523.
- [46] S.E. Esfahani, I. Ghamarian, V.I. Levitas, P.C. Collins, Microscale phase field modeling of the martensitic transformation during cyclic loading of NiTi single crystal, Int. J. Solids Struct. 146 (2018) 80–96.
- [47] H. Babaei, V.I. Levitas, Finite-strain scale-free phase-field approach to multivariant martensitic phase transformations with stress-dependent effective thresholds, J. Mech. Phys. Solids 144 (2020) 104114.
- [48] V.I. Levitas, Elastic model for stress tensor-induced martensitic transformation and lattice instability in silicon under large strains, Mater. Res. Lett. 5 (8) (2017) 554–561, http://dx.doi.org/10.1080/21663831.2017.1362054.
- [49] R. Hill, On Macroscopic Effects Of Heterogeneity In Elastoplastic Media At Finite Strain, Math. Proc. Camb. Phil. Soc. (ISSN: 14698064) 95 (3) (1984) 481–494, http://dx.doi.org/10.1017/S0305004100061818.
- [50] V.I. Levitas, Some relations for finite inelastic deformation of microheterogeneous materials with moving discontinuity surfaces, in: A. Pineau, A. Zaoui (Eds.), IUTAM Symposium on Micromechanics of Plasticity and Damage of Multiphase Materials, Springer Netherlands, Dordrecht, ISBN: 978-94-009-1756-9, 1996, pp. 313-320.
- [51] H. Petryk, Macroscopic rate-variables in solids undergoing phase transformation, J. Mech. Phys. Solids (ISSN: 00225096) 46 (5) (1998) 873–894, http://dx.doi. org/10.1016/S0022-5096(97)00099-9.
- [52] J.D. Schall, G. Gao, J.A. Harrison, Elastic constants of silicon materials calculated as a function of temperature using a parametrization of the second-generation reactive empirical bond-order potential, Phys. Rev. B 77 (11) (2008) 115209.
- [53] W. Bangerth, R. Hartmann, G. Kanschat, deal.IIA general-purpose object-oriented finite element library, ACM Trans. Math. Softw. (ISSN: 00983500) 33 (4) (2007) http://dx.doi.org/10.1145/1268776.1268779.
- [54] M.A. Groeber, M.A. Jackson, DREAM. 3D: A digital representation environment for the analysis of microstructure in 3D, Integr. Mater. Manuf. Innov. 3 (1) (2014) 56–72.
- [55] Y. Jin, A. Artemev, A. Khachaturyan, Three-dimensional phase field model of low-symmetry martensitic transformation in polycrystal: simulation of ζ 2 martensite in AuCd alloys, Acta Mater. 49 (12) (2001) 2309–2320.
- [56] A. Yamanaka, T. Takaki, Y. Tomita, Elastoplastic phase-field simulation of martensitic transformation with plastic deformation in polycrystal, Int. J. Mech. Sci. 52 (2) (2010) 245–250.
- [57] D.C. Wallace, Thermodynamics of crystals, Amer. J. Phys. 40 (11) (1972) 1718–1719.
- [58] J. Wang, S. Yip, S. Phillpot, D. Wolf, Crystal instabilities at finite strain, Phys. Rev. Lett. 71 (25) (1993) 4182.
- [59] T. Barron, M. Klein, Second-order elastic constants of a solid under stress, Proc. Phys. Soc. 85 (3) (1965) 523.
- [60] D.C. Wallace, Thermoelasticity of stressed materials and comparison of various elastic constants, Phys. Rev. 162 (3) (1967) 776.
- [61] V.I. Levitas, Nonlinear elasticity of prestressed single crystals at high pressure and various elastic moduli, Phys. Rev. B 104 (21) (2021) 214105.
- [62] Z. Zeng, Q. Zeng, M. Ge, B. Chen, H. Lou, X. Chen, J. Yan, W. Yang, H.-k. Mao, D. Yang, et al., Origin of plasticity in nanostructured silicon, Phys. Rev. Lett. 124 (18) (2020) 185701.
- [63] Y. Xuan, L. Tan, B. Cheng, F. Zhang, X. Chen, M. Ge, Q. Zeng, Z. Zeng, Pressure-induced phase transitions in nanostructured silicon, J. Phys. Chem. C 124 (49) (2020) 27089–27096.
- [64] S.H. Tolbert, A.B. Herhold, L.E. Brus, A. Alivisatos, Pressure-induced structural transformations in Si nanocrystals: surface and shape effects, Phys. Rev. Lett. 76 (23) (1996) 4384.
- [65] G. Olson, M. Cohen, Dislocation theory of martensitic transformations, in: Dislocations in Solids, North-Holland, 1986, pp. 295–407.

H. Babaei et al.

- [66] V.I. Levitas, S.E. Esfahani, I. Ghamarian, Scale-Free Modeling of Coupled Evolution of Discrete Dislocation Bands and Multivariant Martensitic Microstructure, Phys. Rev. Lett. (ISSN: 10797114) 121 (20) (2018) 205701, http://dx.doi.org/10.1103/PHYSREVLETT.121.205701/FIGURES/4/MEDIUM.
- [67] S.E. Esfahani, I. Ghamarian, V.I. Levitas, Strain-induced multivariant martensitic transformations: A scale-independent simulation of interaction between localized shear bands and microstructure, Acta Mater. (2020) 430–443.
- [68] M. Li, Q. Sun, Nanoscale phase transition behavior of shape memory alloys closed form solution of 1D effective modelling, J. Mech. Phys. Solids 110 (2018) 21–37.
- [69] A. Malik, H.K. Yeddu, G. Amberg, A. Borgenstam, J. Ågren, Three dimensional elasto-plastic phase field simulation of martensitic transformation in polycrystal, Mater. Sci. Eng. A 556 (2012) 221–232.
- [70] A. Malik, G. Amberg, A. Borgenstam, J. Ågren, Phase-field modelling of martensitic transformation: the effects of grain and twin boundaries, Modelling Simul. Mater. Sci. Eng. 21 (8) (2013) 085003.
- [71] T.W. Heo, L.-Q. Chen, Phase-field modeling of displacive phase transformations in elastically anisotropic and inhomogeneous polycrystals, Acta Mater. 76 (2014) 68–81

- [72] H. Xiang, W. Van Paepegem, L. Kestens, Phase-field simulation of martensitic transformation with different conditions in inhomogeneous polycrystals, Comput. Mater. Sci. 220 (2023) 112067.
- [73] V.I. Levitas, M. Javanbakht, Surface tension and energy in multivariant martensitic transformations: phase-field theory, simulations, and model of coherent interface, Phys. Rev. Lett. 105 (16) (2010) 165701.
- [74] V.I. Levitas, M. Javanbakht, Surface-induced phase transformations: multiple scale and mechanics effects and morphological transitions, Phys. Rev. Lett. 107 (17) (2011) 175701.
- [75] V.I. Levitas, Effect of the ratio of two nanosize parameters on the phase transformations, Scr. Mater. 149 (2018) 155–162.
- [76] V.I. Levitas, M. Javanbakht, Phase transformations in nanograin materials under high pressure and plastic shear: nanoscale mechanisms, Nanoscale 6 (1) (2014) 162–166.
- [77] M. Javanbakht, V.I. Levitas, Nanoscale mechanisms for high-pressure mechanochemistry: A phase field study, J. Mater. Sci. (ISSN: 1573-4803) 53 (19) (2018) 13343–13363, http://dx.doi.org/10.1007/S10853-018-2175-X.
- [78] M. Javanbakht, V.I. Levitas, Phase field simulations of plastic strain-induced phase transformations under high pressure and large shear, Phys. Rev. B 94 (2016) 214104, http://dx.doi.org/10.1103/PhysRevB.94.214104.